Article

Cell Metabolism

Mitochondrial DNA Replication Defects Disturb Cellular dNTP Pools and Remodel One-Carbon Metabolism

Graphical Abstract

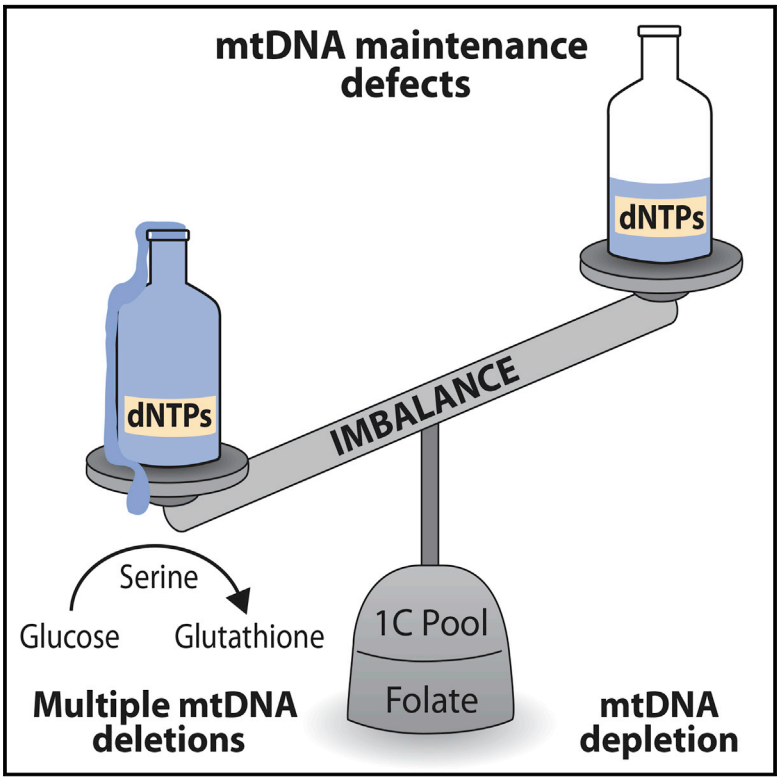

Highlights

- mtDNA replication dysfunction disturbs the cellular folate-driven one-carbon cycle
- mtDNA depletion disorders show low and imbalanced dNTP pools
- Multiple mtDNA deletion disorders show imbalanced and high dNTP pools
- De novo serine biosynthesis drives glutathione production in mitochondrial disease

Authors

Joni Nikkanen, Saara Forsström, Liliya Euro, ..., Vidya Velagapudi, Christopher J. Carroll, Anu Suomalainen

Correspondence

christopher.carroll@helsinki.fi (C.J.C.), anu.wartiovaara@helsinki.fi (A.S.)

In Brief

Nikkanen et al. report that mtDNA replication defects induce a cell-autonomous metabolic stress response in mice, with a widespread imbalance of folate-dependent biosynthetic pathways, including mutagenic dNTP pools, upregulated de novo serine and glutathione synthesis, and deficient metabolite methylation. One-carbon metabolic remodeling is also observed in human patients.

Nikkanen et al., 2016, Cell Metabolism *23*, 1–14
April 12, 2016
http://dx.doi.org/10.1016/j.cmet.2016.01.019

CellPress

Please cite this article in press as: Nikkanen et al., Mitochondrial DNA Replication Defects Disturb Cellular dNTP Pools and Remodel One-Carbon Metabolism, Cell Metabolism (2016), http://dx.doi.org/10.1016/j.cmet.2016.01.019

Cell Metabolism
Article

Mitochondrial DNA Replication Defects Disturb Cellular dNTP Pools and Remodel One-Carbon Metabolism

Joni Nikkanen,[1] Saara Forsström,[1] Liliya Euro,[1] Ilse Paetau,[1] Rebecca A. Kohnz,[2] Liya Wang,[3] Dmitri Chilov,[1] Jenni Viinamäki,[4] Anne Roivainen,[5,6] Päivi Marjamäki,[5] Heidi Liljenbäck,[5,6] Sofia Ahola,[1] Jana Buzkova,[1] Mügen Terzioglu,[1] Nahid A. Khan,[1] Sini Pirnes-Karhu,[1] Anders Paetau,[7] Tuula Lönnqvist,[8] Antti Sajantila,[4] Pirjo Isohanni,[1,8] Henna Tyynismaa,[1,10] Daniel K. Nomura,[2] Brendan J. Battersby,[1] Vidya Velagapudi,[11] Christopher J. Carroll,[1,*] and Anu Suomalainen[1,9,12,*]

[1]Research Programs Unit, Molecular Neurology, University of Helsinki, 00290 Helsinki, Finland
[2]Departments of Chemistry and Nutritional Sciences and Toxicology, University of California, Berkeley, Berkeley, CA 94720, USA
[3]Department of Anatomy, Physiology, and Biochemistry, Swedish University of Agricultural Sciences, 75007 Uppsala, Sweden
[4]Department of Forensic Medicine, University of Helsinki, 00300 Helsinki, Finland
[5]Turku PET Centre, University of Turku, 20520 Turku, Finland
[6]Turku Center for Disease Modeling, Institute of Biomedicine, University of Turku, 20520 Turku, Finland
[7]HUSLAB and Department of Pathology
[8]Department of Child Neurology, Children's Hospital
[9]Department of Neurology
University of Helsinki, Helsinki University Hospital, 00290 Helsinki, Finland
[10]Department of Medical and Clinical Genetics, University of Helsinki, 00290 Helsinki, Finland
[11]Metabolomics Unit, Institute for Molecular Medicine Finland, University of Helsinki, 00290 Helsinki, Finland
[12]Neuroscience Center, University of Helsinki, 00790 Helsinki, Finland
*Correspondence: christopher.carroll@helsinki.fi (C.J.C.), anu.wartiovaara@helsinki.fi (A.S.)
http://dx.doi.org/10.1016/j.cmet.2016.01.019

SUMMARY

Mitochondrial dysfunction affects cellular energy metabolism, but less is known about the consequences for cytoplasmic biosynthetic reactions. We report that mtDNA replication disorders caused by TWINKLE mutations—mitochondrial myopathy (MM) and infantile onset spinocerebellar ataxia (IOSCA)—remodel cellular dNTP pools in mice. MM muscle shows tissue-specific induction of the mitochondrial folate cycle, purine metabolism, and imbalanced and increased dNTP pools, consistent with progressive mtDNA mutagenesis. IOSCA-TWINKLE is predicted to hydrolyze dNTPs, consistent with low dNTP pools and mtDNA depletion in the disease. MM muscle also modifies the cytoplasmic one-carbon cycle, transsulfuration, and methylation, as well as increases glucose uptake and its utilization for de novo serine and glutathione biosynthesis. Our evidence indicates that the mitochondrial replication machinery communicates with cytoplasmic dNTP pools and that upregulation of glutathione synthesis through glucose-driven de novo serine biosynthesis contributes to the metabolic stress response. These results are important for disorders with primary or secondary mtDNA instability and offer targets for metabolic therapy.

INTRODUCTION

Mitochondria are versatile organelles that participate in cellular catabolic and anabolic pathways. Upon increased energy demand or fasting, they efficiently burn nutrients to synthesize ATP, whereas, in a fed state, they provide cofactors and metabolites for cell growth. The metabolic shifts and the downstream biosynthetic pathways are tightly regulated by the redox status, which changes depending on nutrient availability and mitochondrial function (Nunnari and Suomalainen, 2012). However, little is known about the consequences of mitochondrial pathology for cytoplasmic biosynthetic pathways.

Mitochondrial disorders are caused by defects in either mtDNA encoding 13 proteins of oxidative phosphorylation or, in ~1,300 nuclear genes, encoding mitochondrion-targeted proteins (Pagliarini et al., 2008; Pagliarini and Rutter, 2013). The disorders show exceptionally variable phenotypes ranging from infantile multi-tissue disorders to adult-onset progressive degeneration of the heart, muscle, brain, or sensory organs. Even mutations in a single gene can cause distinct manifestations, implicating considerable functional complexity of mitochondrial proteins (Hakonen et al., 2005; Naviaux et al., 1999; Van Goethem et al., 2004). Dominant mutations of TWINKLE, the replicative mtDNA helicase (Korhonen et al., 2004; Spelbrink et al., 2001), manifest as adult-onset mitochondrial myopathy (MM) (also called progressive external ophthalmoplegia [PEO]) with multiple mtDNA deletions in post-mitotic tissues (Suomalainen et al., 1992; Zeviani et al., 1989), whereas recessive mutations of TWINKLE (Nikali et al., 2005) cause mtDNA depletion in the brain and liver (Hakonen et al., 2008), manifesting as

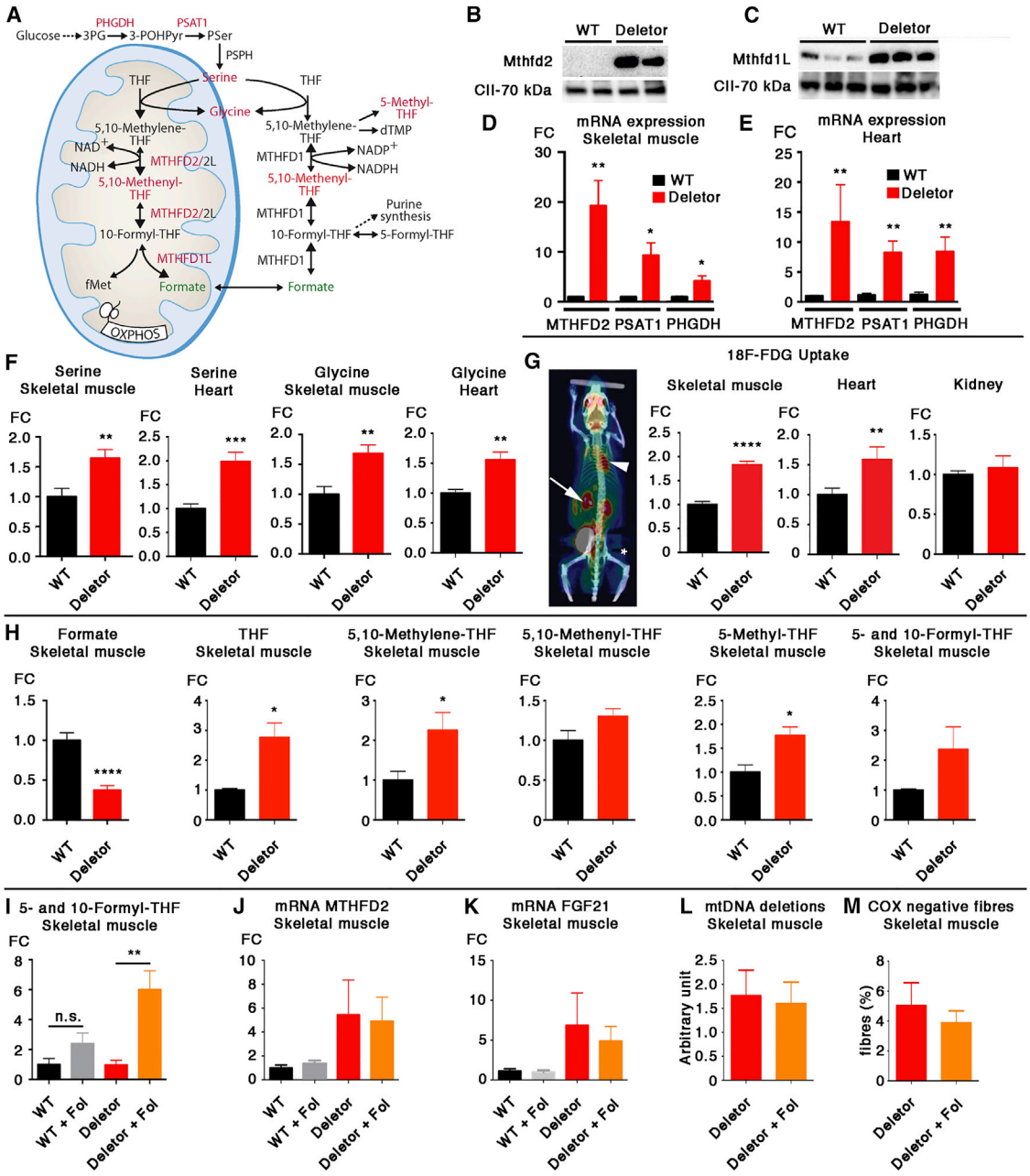

Figure 1. Imbalanced Mitochondrial and Cytoplasmic Folate Cycle in Mitochondrial Myopathy

(A) Schematic of the mitochondrial and cytoplasmic folate cycle and summary of findings in Deletor muscle. Red text, increased amount; green, decreased amount of metabolites/cofactors/proteins in Deletor muscle. PSPH, phosphoserine phosphatase; dTMP, deoxy thymidine monophosphate; 3-PG, 3-phosphoglycerate; 3-POHPyr, 3-phosphohydroxypyruvate; PSer, phosphoserine; fMet, formylmethionine; OXPHOS, oxidative phosphorylation; NADH, NAD+, nicotinamide adenine dinucleotide; PHGDH, phosphoglycerate dehydrogenase; PSAT1, phosphoserine aminotransferase; THF, tetrahydrofolate; MTHFD, methylene-tetrahydrofolate dehydrogenase.

(B and C) MTHFD2 (B) and MTHFD1L (C) protein amounts in skeletal muscle. Shown are western blot analyses of Deletor and wild-type (WT) mice. Respiratory chain complex II (70-kDa subunit) served as a loading control for mitochondrial protein.

(D and E) mRNA expression levels of *Mthfd2* and the serine de novo biosynthesis enzymes *Phgdh* and *Psat1* in skeletal muscle (D) and heart (E) (n = 6).

(F) Serine and glycine concentrations in skeletal muscle (WT, n = 10; Deletor, n = 9) and heart (WT, n = 7; Deletor, n = 8). Ultra performance liquid chromatography and triple-quadrupole mass spectrometry were used.

(G) In vivo glucose uptake by mouse tissues as determined by [^{18}F]fluoro-2-deoxy-D-glucose labeling and positron emission tomography. The arrow indicates the [^{18}F]FDG signal in the kidney, the arrowhead that in the heart, and the asterisk that in the quadriceps femoris muscle. Right: signal quantification (WT, n = 6; Deletor, n = 5).

(H) Folate intermediate concentrations in skeletal muscle (male; WT, n = 5; Deletor, n = 6) were determined by UPLC-MS/MS analysis (except formate) of tissue extracts. Formate concentration (WT n = 5, Deletor n = 9) was determined by gas chromatography-mass spectrometry analysis.

(legend continued on next page)

infantile onset spinocerebellar ataxia (IOSCA; progressive cerebellar ataxia, peripheral and optic neuropathy, hearing loss, athetosis, female hypergonadotropic hypogonadism, epilepsy, and hepatopathy), but no muscle symptoms or signs (Lönnqvist et al., 1998). The molecular mechanistic basis of the tissue specificity of mtDNA maintenance disorders is unknown.

The "Deletor" mouse is a model for adult-onset MM with multiple mtDNA deletions (Tyynismaa et al., 2005). These mice carry a dominant TWINKLE defect, homologous to a patient mutation that induced a widespread transcriptional response of genes with an amino acid response element in their upstream regulatory region (Tyynismaa et al., 2010). One of these transcripts was methylenetetrahydrofolate dehydrogenase 2 (*Mthfd2*), a bi-functional enzyme of mitochondrial folate metabolism (Di Pietro et al., 2004). The folate cycle, operating in mitochondria and cytoplasm, shuttles one-carbon (1C) units to 1C-dependent biosynthetic pathways, including nucleotide synthesis and methylation reactions (Christensen and MacKenzie, 2006; Jain et al., 2012; Nilsson et al., 2014). Distinct folates feed separate biosynthetic pathways that compete for a limiting common cofactor pool (Schirch and Strong, 1989; Scott and Weir, 1981; Strong et al., 1990; Suh et al., 2001). The strong induction of *Mthfd2* in Deletor mice raised the question of whether 1C-dependent metabolism could contribute to the pathogenesis of mitochondrial disorders.

Here we report that mtDNA maintenance disease results in whole cellular nucleotide imbalance. This is associated with widespread changes in cytoplasmic anabolic pathways, with highly induced de novo serine biosynthesis, glutathione synthesis, transsulfuration, and a concomitant aberrant methyl cycle with deficient metabolite methylation. Our evidence suggests that remodeling of 1C metabolism is a likely contributor to mtDNA maintenance disease progression, characterized by mtDNA mutagenesis and/or depletion. The cell-autonomous aberration of biosynthetic pathways as a consequence of mtDNA instability implies that the mechanisms also have relevance for conditions with secondary mtDNA instability, such as Parkinson's disease and aging.

RESULTS

Mitochondrial Myopathy Induces Mitochondrial 1C Metabolism and Serine Biosynthesis

We have previously reported the induction of an amino acid starvation response in the Deletor mouse muscle, including prominent induction of MTHFD2, correlating with disease severity (Tyynismaa et al., 2010). MTHFD2 is expressed at low levels in post-mitotic tissues of healthy adults, which suggested a role for the mitochondrial folate cycle compartment in mitochondrial disease. The cycle produces formyl-methionine for mitochondrial translation, nicotinamide adenine dinucleotide phosphate (NADPH) for membrane synthesis, and formate, which is the major 1C donor for cytoplasmic purine synthesis (Figure 1A; Tibbetts and Appling, 2010). We show here that two key enzymes of the mitochondrial 1C cycle, MTHFD2 and MTHFD1L, were induced in the Deletor muscle, but no change in *Shmt2* gene expression was detected (Figures 1B–1E; Figure S1A). Serine is the primary 1C donor for the mitochondrial folate cycle, donating its side-chain carbon to folate, which generates glycine and methylene-tetrahydrofolate, entering the 1C cycle. Serine can be imported to cells from extracellular sources or made de novo by diverting 3-phosphoglycerate from the glycolytic pathway to the 1C cycle by phosphoglycerate dehydrogenase (PHGDH) (Locasale et al., 2011). We found both serine and glycine concentrations to be increased 1.5- to 2-fold in Deletor muscle and heart (Figure 1F), with 5- to 10-fold increased gene expression of enzymes of the de novo serine biosynthesis pathway, PHGDH and phosphoserine aminotransferase (PSAT1) (Figures 1D and 1E). Also, the in vivo uptake of glucose (2-[^{18}F]fluoro-2-deoxy-*D*-glucose [FDG] positron emission tomography [PET]/computed tomography [CT]), the primary substrate of de novo serine biosynthesis, was high in Deletor skeletal muscle and heart (Figure 1G). We found no signs of increased serine in Deletor liver and brain (Figure S1B). These data indicate a strong induction of the mitochondrial compartment of the 1C cycle specifically in the affected tissues in mtDNA maintenance disease.

Mitochondrial and Cytoplasmic 1C Cycle Imbalance in Mitochondrial Disease

To understand whether the remarkable induction of mitochondrial folate cycle enzymes affected the total cellular folate pools, we established a mass spectrometric analysis for specific folate intermediates that serve different biosynthetic reactions (Figure 1H; Figure S1C). Different tetrahydrofolate (THF) intermediates showed significant increases in male Deletor muscle (Figure 1H), and similar but more subtle changes were present in female Deletors, which showed a slightly slower progression of MM disease than males (Tyynismaa et al., 2010). In males, formate, the product of MTHFD1L and substrate for purine synthesis, was 30% that of the wild-type (WT) level, but THF forms showed induction, with increased 5-methyl-THF, 5,10-methylene-THF, and THF amounts. In female Deletors, 5-methyl-THF, which is the cofactor donating 1C units for methylation reactions, and 5,10-methenyl-THF, produced by MTHFD2 and regulating 1C flow toward purine metabolism (Field et al., 2006), were elevated 1.5-fold (Figure S1C). These findings indicate a remarkable steady-state imbalance of folate cycle intermediates and are consistent with the increased demand of 1C units for purine and methionine synthesis in mtDNA replication disease.

Folinic Acid Supplementation Does Not Reverse Disease Pathology

The marked upregulation of the mitochondrial folate cycle as well as the imbalance of whole cellular folate species raised the question of whether folate supplementation would be beneficial for

(I) Folinic acid (Fol) supplementation effects. Shown is the 5- and 10-formyl-THF level in skeletal muscle of WT and Deletor mice after 8-week supplementation with folinic acid (n = 5 mice/group).

(J and K) Folinic acid supplementation effects and mRNA expression. *Mthfd2* (J) and *Fgf21* (K) in Deletor skeletal muscle after 8-week supplementation (n = 5 mice/group, qPCR).

(L and M) mtDNA deletion load (L) and number of COX-deficient muscle fibers (M) after folinic acid supplementation (n = 5 mice/group).

All data are presented as mean, and error bars indicates SEM. *p < 0.05, **p < 0.01, ***p < 0.001, ****p < 0.0001. See also Figure S1.

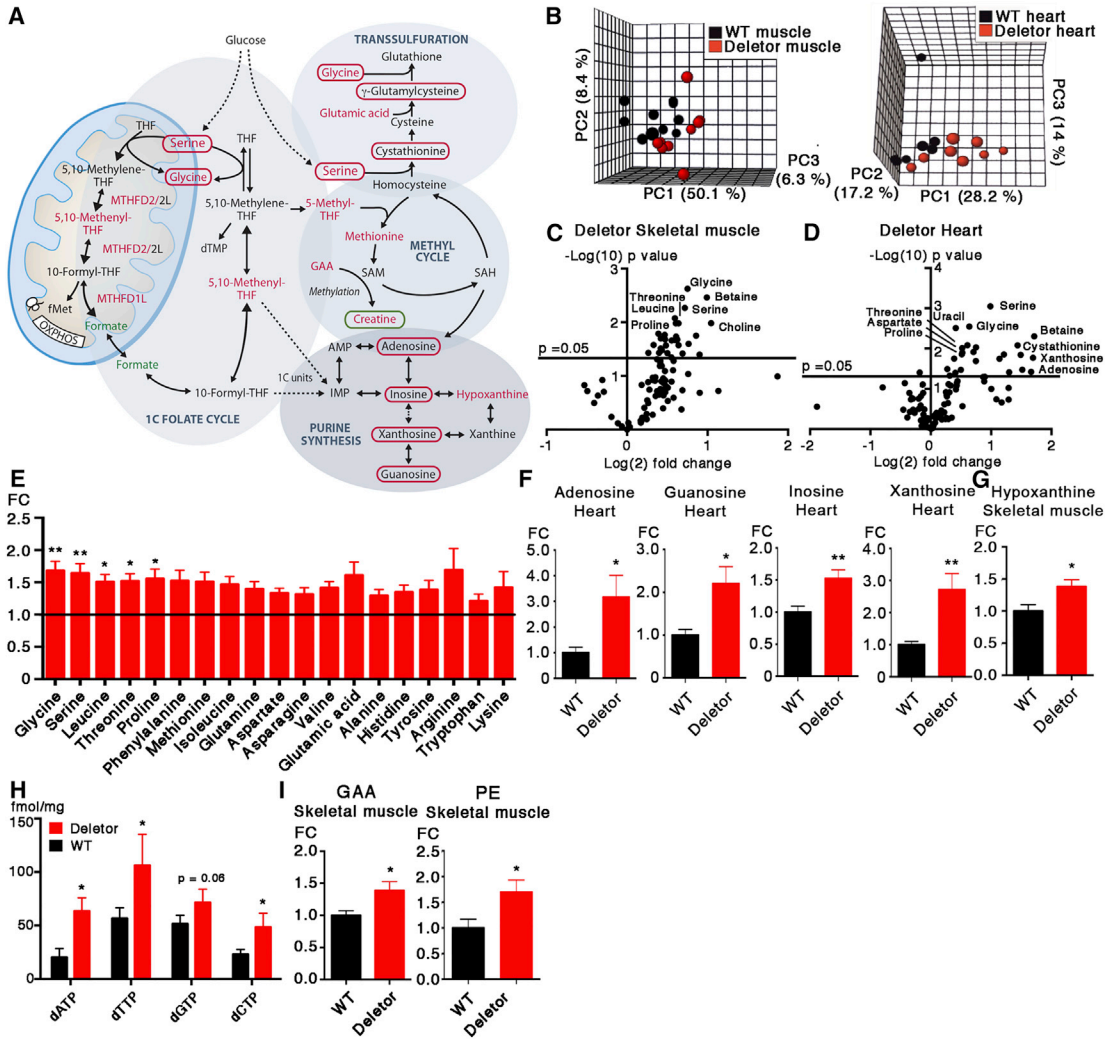

Figure 2. Aberrant Cytoplasmic 1C Metabolism in Mitochondrial Myopathy

(A) 1C metabolism and aberrant pathways in Deletor skeletal muscle and heart. Circled metabolites, changed in heart; colored text, changed in muscle; red, increase; green: decrease. SAH, S-adenosyl homocysteine; SAM, S-adenosyl methionine; IMP, AMP, inosine/adenosine monophosphate; GAA, guanidino-acetic acid.

(B) Unsupervised principal component analysis (PCA) of metabolome data from Deletor muscle and heart.

(C and D) Volcano plots of analyzed metabolites in Deletor skeletal muscle and heart. Full lists of changed metabolites can be found in Tables S2 and S3.

(E) Amino acid levels in Deletor muscle (Deletor, n = 8; WT, n = 7).

(F) Purine metabolites changed significantly in the heart (Deletor, n = 8; WT, n = 7).

(G) Hypoxanthine amount in Deletor muscle (Deletor, n = 9; WT, n = 10).

(H) dNTP concentrations in skeletal muscle (Deletor, n = 5; WT, n = 8).

(I) Unmethylated metabolites of creatine and phosphatidylcholine synthesis (guanidino-acetic acid, phosphatidylethanolamine).

All data are presented as mean, and error bars indicate SEM. *p < 0.05, **p < 0.01. See also Figure S2; Tables S1, S2, and S3.

disease pathology. We supplemented 22-month-old Deletors with advanced disease and their WT littermates with folinic acid (5-formyl-THF), the active storage folate form. Eight weeks of supplementation significantly increased the 5-formyl-THF concentration 6-fold in Deletor muscle, whereas, in the WT, the amount increased 2-fold. The increase indicated successful and enhanced delivery of the compound to the affected tissue (Figure 1I). However, the increased cofactor availability did not affect disease-associated changes (*Mthfd2*, *Fgf21* expression levels, mutant mtDNA amount, and cytochrome *c* oxidase (COX)-negative fibers; Figures 1J–1M). These data indicate that the pathology-associated folate cycle changes are not improved by nutritional folate availability.

The Metabolome of mtDNA Maintenance Disease Indicates an Alternative 1C Donor and Purine Biosynthesis Induction

The aberrant cytoplasmic and mitochondrial folate cycle predicted changes in the major biosynthetic pathways, purine synthesis, methyl cycle, and transsulfuration (Figure 2A), sharing the limited 1C pool. This prompted us to undertake a high-throughput quantitative analysis of 109 metabolites of Deletor

muscle and heart (Table S1). Unsupervised clustering indicated genotype-specific clustering (Figure 2B). The altered metabolites indicated a widespread increase of amino acid concentrations, especially serine and glycine, which are known cellular donors of 1C units. Elevated concentrations of threonine and betaine, which indirectly connect to folate and methyl cycles, suggest the induction of alternative 1C sources to replenish the 1C pool (Figures 2C–2E). In the Deletor heart, the purine degradation products adenosine, guanosine, inosine, and xanthosine were especially increased (1.5- to 3-fold; Figure 2F), and more modest but significant changes of hypoxanthine were present in Deletor skeletal muscle (Figure 2G). These findings strongly suggest that a primary mtDNA replication defect modified a major cytoplasmic anabolic pathway, purine metabolism.

mtDNA Maintenance Defects Disturb dNTP Pools

Because of the steady-state purine metabolic aberrations and because pyrimidines were not well represented in our targeted metabolomics screening, we directly measured whole cellular deoxynucleotide triphosphate (dNTP) pools, the end products of purine and pyrimidine synthesis, in Deletor skeletal muscle. The pools were remarkably increased and imbalanced, with deoxyadenosine triphosphate (dATP) showing 3-fold, deoxythymidine triphosphate (dTTP) and deoxycytidine triphosphate (dCTP) 2-fold, and deoxyguanosine triphosphate (dGTP) 1.3-fold increased concentrations compared with WT littermates (Figure 2H). Imbalanced and increased dNTP pools are well known to be genotoxic in dividing cells (Garcia-Diaz et al., 2014).

mtDNA replication is the major user of cytoplasmic dNTPs in post-mitotic tissues (Bourdon et al., 2007), and imbalanced dNTP pools would therefore primarily induce mtDNA mutagenesis. Deletor mice show progressive mutagenesis as multiple mtDNA deletions accumulate in their skeletal muscle and heart (Figure S2A), along with the disease progression in mice and patients. Our next-generation mtDNA sequencing analysis of Deletor muscle did not indicate an increased mtDNA point mutation rate (Figure S2B), which may be explained by the high fidelity of the mtDNA polymerase, with an accurate exonuclease function. These results are consistent with altered dNTP pools accelerating mtDNA mutagenesis in disorders with multiple mtDNA deletions.

mtDNA Maintenance Defects Lead to Insufficient Metabolite Methylation

The folate cycle also feeds the methyl cycle, a major 1C-dependent biosynthetic pathway, accepting 1C units from 5-methyl-THF for methionine synthesis. The methylation capacity is especially used for metabolite methylation, of which creatine and phosphatidylcholine (PC) synthesis utilizes the vast majority—up to 80%. Creatine synthesis occurs when guanidinoacetate methyltransferase (GAMT) methylates guanidino-acetic acid (GAA) in an S-adenosylmethionine (SAM)-dependent reaction (García-Martínez and Appling, 1993; Pike et al., 2010), and PC synthesis involves the methylation of phosphatidylethanolamine (PE). To find out whether the methyl cycle was affected by the imbalanced folate pools, we analyzed both creatine and PC synthesis. The precursors of both were increased in Deletor muscle: GAA +1.5-fold and PE +1.7-fold (Figure 2I). No major changes in total genomic DNA methylation, a minor user of the methyl pool, were present in Deletor muscle ($p = 0.44$). These results strongly point to an aberrant methyl cycle and insufficient methylation capacity for creatine and PC synthesis in skeletal muscle, the major site of creatine synthesis in adult age, upon mtDNA replication disease.

[U-^{13}C]-Glucose Flux toward De Novo Synthesis of Serine and Glutathione in Deletor Mice

The considerable changes in steady-state de novo serine biosynthesis and 1C-dependent pathways in mitochondrial disease raised the question of the direction of metabolic flux. First we established that Deletor heart and skeletal muscle showed increased [^{18}F]FDG uptake, measured by PET/ CT analysis (Figure 1G). To directly assess the metabolic flux in vivo, we administered uniformly **[**U-^{13}C**]**-labeled glucose to Deletor and WT mouse tail veins and followed the primary biosynthetic incorporation of glucose-derived carbons into downstream metabolites. Because of the prominent upregulation of the serine de novo biosynthesis pathway, we chose the chase time point of 15 min, during which serine labeling was in the linear phase (Figure S3A). The Deletor heart showed the most significant changes, although, at the specific time point, the skeletal muscle labeling was not yet significant. Oxidative metabolism of the fully labeled glucose resulted in fully **[**U-^{13}C**]**-labeled serine (three carbons, m+3), the amount of which was increased 2-fold compared with WT mice (Figure 3A). Glutathione (m+5) labeling was also increased ~2-fold compared with the WT. The glutathione m+5-labeled carbons originate from glucose-derived serine and glycine as well as glutamate. The specific glucose carbons from serine versus glutamate could not be traced, but the overall significant glutathione labeling demonstrates increased glutathione biosynthesis.

Serine is a substrate for cystathionine synthesis in transsulfuration (Figure 3B). We found increased steady-state levels of cystathionine and γ-glutamylcysteine in the heart, and cystathionine γ-lyase (CTH) was highly induced in Deletor heart and muscle (Figures 3C and 3D). Also, glutamate-cysteine ligase (GCLC) showed increased expression (Figure 3F; Figure S3B) in muscle, which agrees with an increased need of glutathione and flux toward its synthesis upon mtDNA replication defects. Also, glutathione reductase activity was increased, but no change was detected in glutathione peroxidase activity (Figure 3G). This serine-glutathione pathway is highly conserved in species. Analysis with the Clustering of Inferred Models of Evolution (CLIME) program (Li et al., 2014) revealed that PHGDH (the rate-limiting enzyme in de novo serine biosynthesis) closely co-evolved with CTH and cystathionine β-synthase (CBS), the first two enzymes in the transsulfuration pathway (Figures 3B and 3E), which strongly supports a functional interdependence of the pathways.

These data show that mitochondrial dysfunction induces a potential stress pathway in the affected tissues, promoting glucose-driven de novo serine biosynthesis and directing serine to the transsulfuration pathway to synthesize glutathione.

The Recessive TWINKLE Disease Model for IOSCA Shows Aberrant, Low Muscle dNTP Pools

To analyze whether the metabolic changes found in Deletor mice have a role in another model of mtDNA maintenance disease, we generated a mouse model for IOSCA disease, also caused by

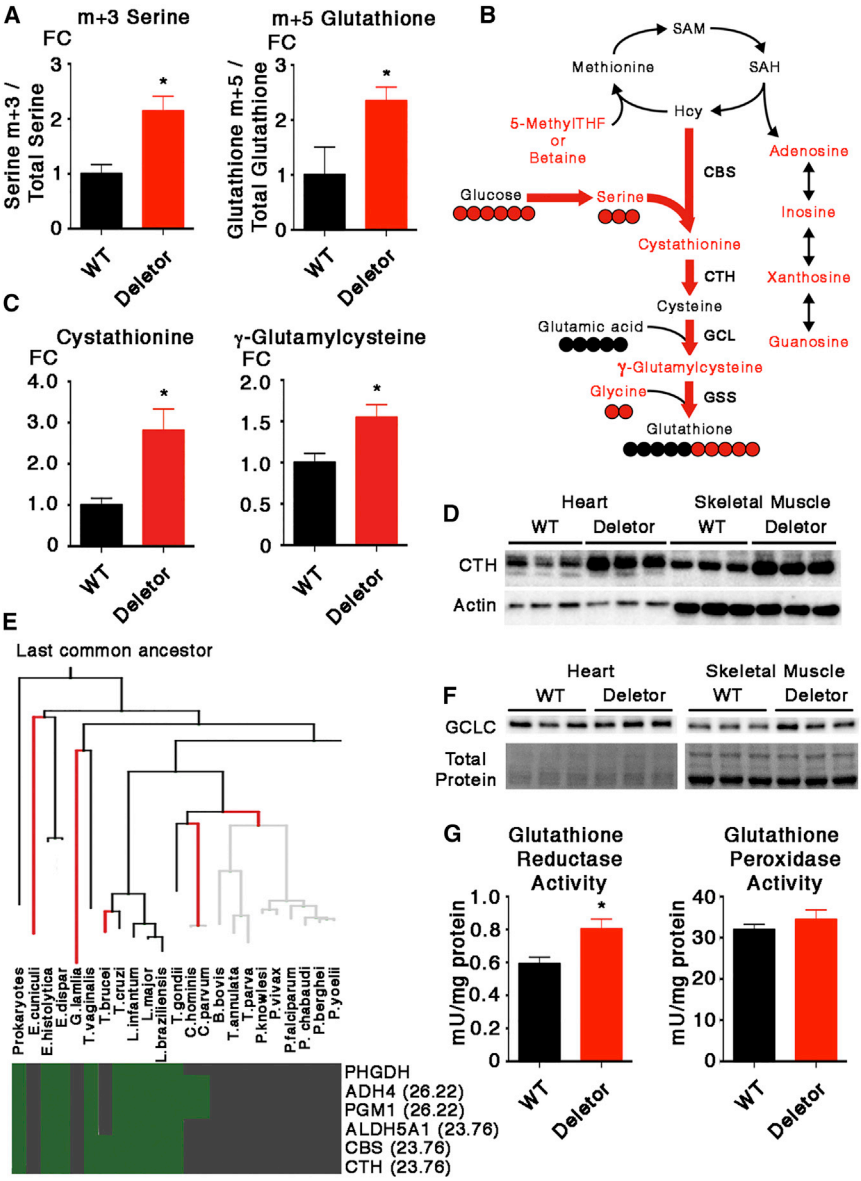

Figure 3. Increased In Vivo Glucose Flux toward Serine and Glutathione Synthesis in Affected Tissues of Mitochondrial Myopathy Mice

(A) Labeled metabolites in WT (n = 4) and Deletor (n = 4) hearts after administration of [U-^{13}C]-glucose (15-min trace; m+3 and m+5, mass + labeled carbons; quantification against total metabolite amount).

(B) Overview of the methyl cycle and transsulfuration and glutathione synthesis pathways. Red text, increased steady-state concentrations in the Deletor heart; red arrows, glucose flux; red/black circles, labeled versus unlabeled carbons. Hcy, homocysteine; GCL, glutamate-cysteine ligase; GSS, glutathione synthetase; CBS, cystathionine β-synthetase; CTH, cystathionase.

(C) Quantification of steady-state cystathionine (WT, n = 7; Deletor, n = 8) and γ-glutamylcysteine (WT, n = 5; Deletor, n = 5) in the heart.

(D) Expression of CTH in Deletor heart and muscle (western blot).

(E) Evolutionary analysis showing the co-evolving gene module for PHGDH (adapted from CLIME with top 5 hits, gene paralogues excluded). The red line indicates loss of PHGDH. Log-likelihood ratio scores are shown in parentheses.

(F) GCLC expression in Deletor heart and muscle.

(G) Glutathione reductase and peroxidase enzyme activities in WT (n = 5) and Deletor (n = 4) hearts.

ADH4, alcohol dehydrogenase 4; PGM1, phosphoglucomutase 1; ALDH5A1, aldehyde dehydrogenase 5A1. All data are presented as mean, and error bars indicate SEM. *p < 0.05. See also Figure S3.

TWINKLE mutation, but being recessive and causing a severe infantile disease with partial loss of mtDNA, i.e., mtDNA depletion. We inserted a c.1526 A > G mutation in exon 3 of the C10orf2 gene (p.Y508C in human IOSCA patients and p.Y509C in mice) encoding the TWINKLE helicase (Figures 4A–4C). The different genotypes were born in Mendelian proportions. Homozygous IOSCA knockin mice ("IOSCA mice") had decreased mtDNA copy numbers in the liver, but no depletion was detected in other tissues (Figure 4D), and no mtDNA deletions were detected (Figure 4E). At 17 months of age, IOSCA mice consumed more oxygen and produced more CO_2 at thermoneutral temperature (+30°C) compared with their WT littermates (Figure 4F). IOSCA mice weighed less than WT mice from 9 months of age (Figure 4G) but showed no apparent motor or sensory defects (Figures S4A and S4B). At 6 months of age, 5 of 21 male mice manifested with generalized epileptic seizures induced by handling (Movie S1).

Despite the relatively subtle neurological phenotype of the IOSCA mice, their brains showed clear signs of progressive neurodegeneration at 19 months of age. The hippocampal pyramidal neuron layer in the CA1 region showed decreased neurite density and disorganization of the apical dendritic trees (Figures 4H–4J) without a reduction in neuronal number. Other hippocampal regions, deep gray matter nuclei, and cortical neurons showed no changes. Deletor mice (24 months old) had a WT-like cerebellar and hippocampal CA1 neuronal morphology (Figures 4H and 4J). The cerebellar Purkinje neurons of IOSCA mice were decreased in number and showed reduced arborization of the dendritic trees (Figure 4T). These results indicate that cerebellar Purkinje cells were most sensitive to IOSCA mutation, followed by the large neurons of hippocampal CA1, a region implicated in epilepsy. The Purkinje cell changes were not severe enough to manifest as ataxia. Similar to IOSCA patients (Figure S4C), the skeletal muscle of IOSCA mice lacked signs of MM, whereas Deletor mice and MM/PEO patients harbored COX-deficient muscle fibers (Figures 4K–4M; Figure S4D). IOSCA mouse hepatocytes showed degenerative vacuolization indicative of hepatopathy (Figures 4N–4P) and decreased lipid content. Deletor livers also had reduced lipids but no degeneration (Figures 4Q–4S). Fibroblast growth factor 21, secreted by

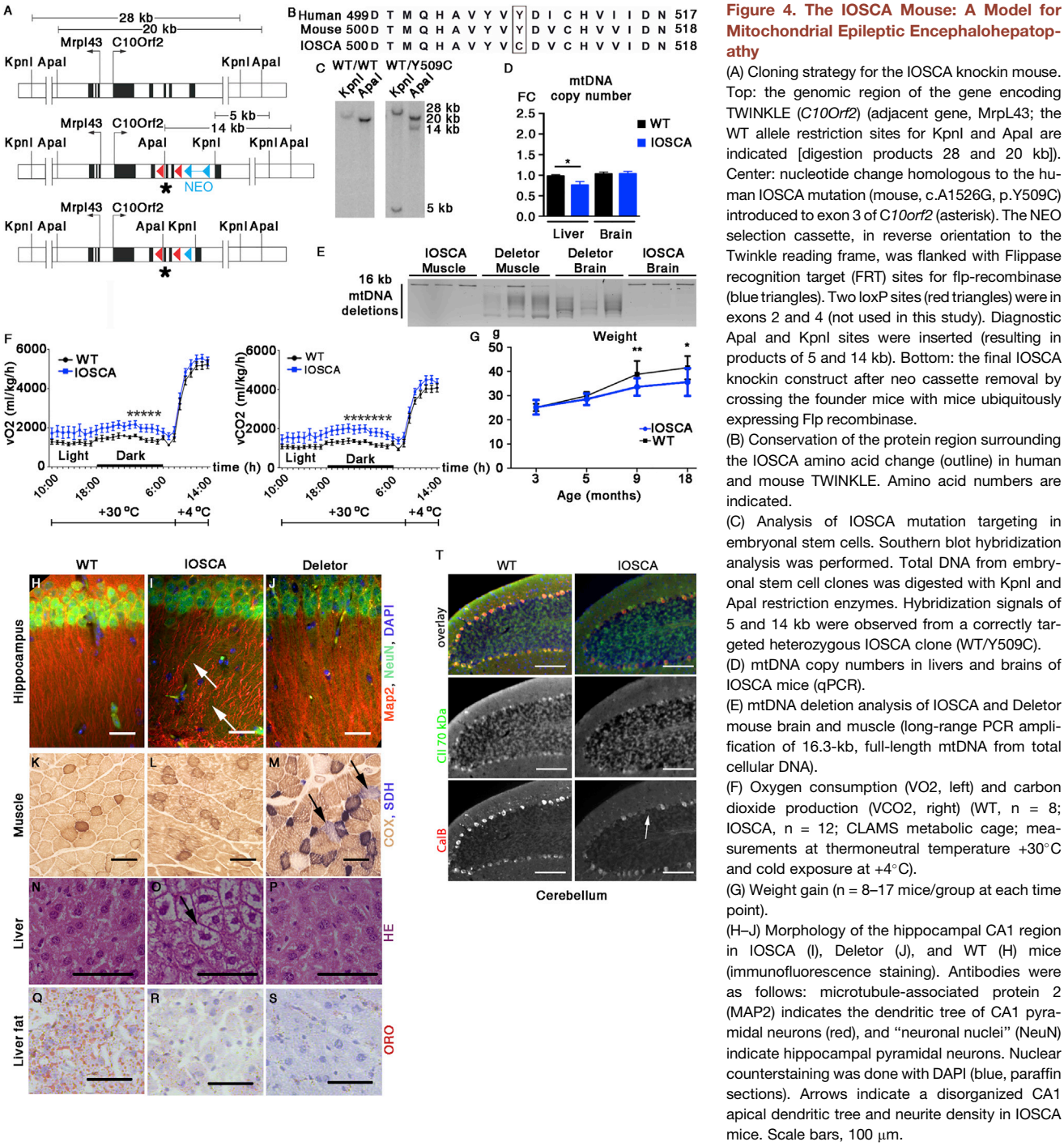

Figure 4. The IOSCA Mouse: A Model for Mitochondrial Epileptic Encephalohepatopathy

(A) Cloning strategy for the IOSCA knockin mouse. Top: the genomic region of the gene encoding TWINKLE (*C10Orf2*) (adjacent gene, MrpL43; the WT allele restriction sites for KpnI and ApaI are indicated [digestion products 28 and 20 kb]). Center: nucleotide change homologous to the human IOSCA mutation (mouse, c.A1526G, p.Y509C) introduced to exon 3 of *C10orf2* (asterisk). The NEO selection cassette, in reverse orientation to the Twinkle reading frame, was flanked with Flippase recognition target (FRT) sites for flp-recombinase (blue triangles). Two loxP sites (red triangles) were in exons 2 and 4 (not used in this study). Diagnostic ApaI and KpnI sites were inserted (resulting in products of 5 and 14 kb). Bottom: the final IOSCA knockin construct after neo cassette removal by crossing the founder mice with mice ubiquitously expressing Flp recombinase.

(B) Conservation of the protein region surrounding the IOSCA amino acid change (outline) in human and mouse TWINKLE. Amino acid numbers are indicated.

(C) Analysis of IOSCA mutation targeting in embryonal stem cells. Southern blot hybridization analysis was performed. Total DNA from embryonal stem cell clones was digested with KpnI and ApaI restriction enzymes. Hybridization signals of 5 and 14 kb were observed from a correctly targeted heterozygous IOSCA clone (WT/Y509C).

(D) mtDNA copy numbers in livers and brains of IOSCA mice (qPCR).

(E) mtDNA deletion analysis of IOSCA and Deletor mouse brain and muscle (long-range PCR amplification of 16.3-kb, full-length mtDNA from total cellular DNA).

(F) Oxygen consumption (VO2, left) and carbon dioxide production (VCO2, right) (WT, n = 8; IOSCA, n = 12; CLAMS metabolic cage; measurements at thermoneutral temperature +30°C and cold exposure at +4°C).

(G) Weight gain (n = 8–17 mice/group at each time point).

(H–J) Morphology of the hippocampal CA1 region in IOSCA (I), Deletor (J), and WT (H) mice (immunofluorescence staining). Antibodies were as follows: microtubule-associated protein 2 (MAP2) indicates the dendritic tree of CA1 pyramidal neurons (red), and "neuronal nuclei" (NeuN) indicate hippocampal pyramidal neurons. Nuclear counterstaining was done with DAPI (blue, paraffin sections). Arrows indicate a disorganized CA1 apical dendritic tree and neurite density in IOSCA mice. Scale bars, 100 μm.

(K–M) Respiratory chain activity in skeletal muscle in IOSCA (L), Deletor (M), and WT (K) mice. Shown is the histochemical analysis of COX (brown) and succinate dehydrogenase (SDH, blue) activities. Arrows indicate COX-deficient muscle fibers (white or blue) (frozen sections). Scale bars, 100 μm.

(N–P) Liver histology in IOSCA (O), Deletor (P), and WT (N) mice (H&E staining, paraffin sections). The arrow indicates vacuolar hepatocyte degeneration in IOSCA mice. Scale bars, 100 μm.

(Q–S) Liver fat content in IOSCA (R), Deletor (S), and WT (Q) mice (oil red O staining [ORO], frozen sections). Red staining indicates lipid (hematoxylin counterstaining). Scale bars, 100 μm.

(T) Cerebellar morphology. Shown is immunofluorescence staining of mid-sagittal sections through the cerebellum of wild-type and IOSCA mice (19 months old). Antibodies used were as follows: calbindin (red in the overlay) indicates Purkinje neurons; respiratory chain complex II (70-kDa subunit) indicates mitochondria (green in overlay). Nuclear DAPI counter staining was performed (blue in the overlay). Paraffin sections were used. The arrow indicates Purkinje cell dropout. Scale bars, 100 μm.

All data are presented as mean, and error bars indicate SEM. *$p < 0.05$, **$p < 0.01$. See also Figure S4 and Movie S1.

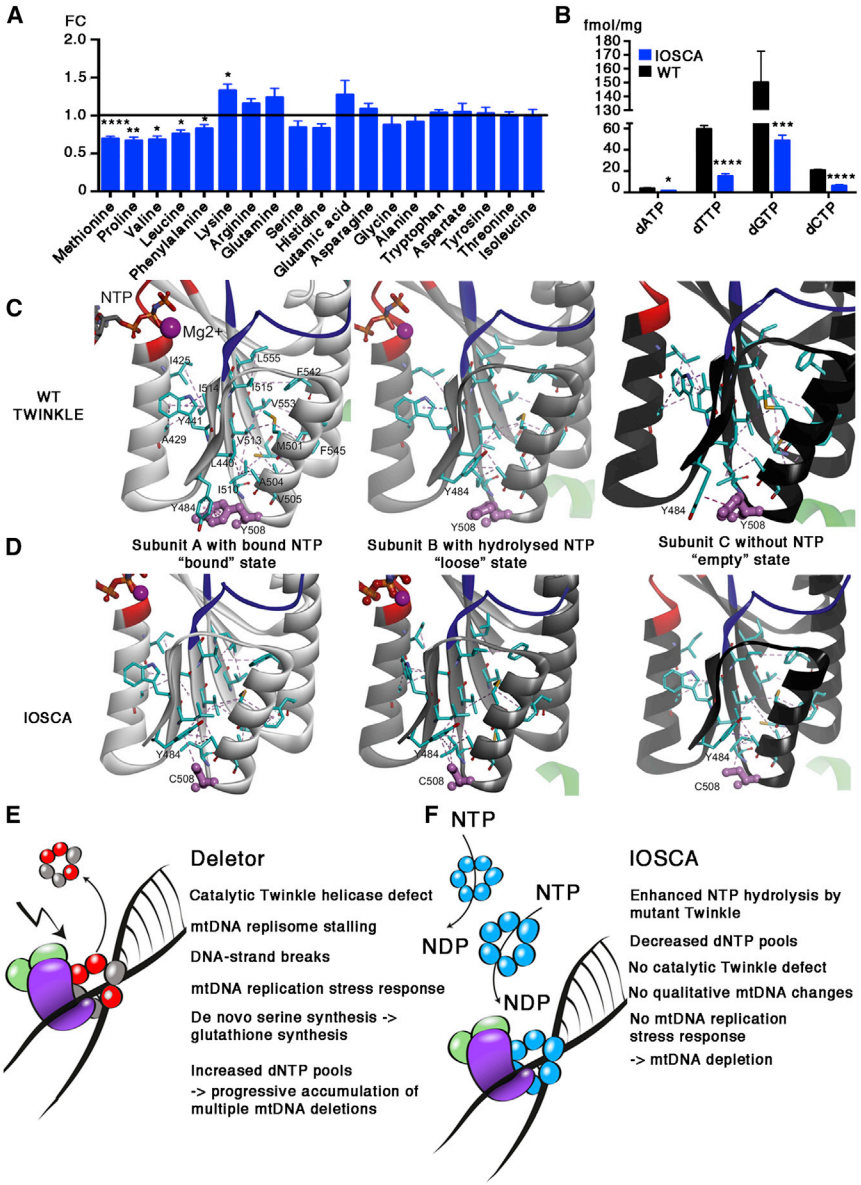

Figure 5. The IOSCA Knockin Mouse Shows Depleted dNTP Pools in Skeletal Muscle

(A) Amino acid levels in IOSCA muscle (IOSCA, n = 8; WT, n = 5; fold change compared with the WT).

(B) dNTP concentrations in skeletal muscle (IOSCA, n = 6; WT, n = 5).

(C) Protein modeling of human WT TWINKLE helicase based on the structure of T7 gene 4 helicase (PDB ID 1E0J). Y508 is shown in purple. Three neighboring subunits (A–C) of human TWINKLE are modeled in sequential catalytic steps. Intrasubunit interactions and their changes within helicase domain couple NTP (red) hydrolysis with ssDNA translocation. As in bacteriophage helicase, ssDNA is bound to only one subunit in the hexamer at the time, and, therefore, each subunit sequentially undergoes the same cycle of catalytic events. Left: catalysis initiation with NTP binding, triggering binding of DNA. Center: DNA initiates NTP hydrolysis, followed by (right) nucleotide diphosphate (NDP) and phosphate (Pi) release and subunit rotation, needed for ssDNA translocation through the central pore of the helicase. Coupling of NTP hydrolysis and DNA movement is maintained by rearrangement of non-covalent bonding in the hydrophobic core of the helicase domain (pink dashed lines). Y508 (pink) is involved in the coupling mechanism. Note the important stacking interaction between Y484 and Y508 in the WT undergoing on/off modes upon the catalytic cycle, driven by ssDNA binding/translocation.

(D) Modeling of TWINKLE helicase with IOSCA amino acid change (Y508C in human and Y509C in mouse). The variant is predicted to modify hydrophobic interactions within the helicase domain, keeping it in an intermediate state between "loose" and "empty." We propose that this flexible conformation is favoring fast DNA-independent NTP hydrolysis and product release.

(E) Model of the pathogenic consequences of dominant TWINKLE mutation underlying mitochondrial myopathy. Mutant helicase leads to replication stalling, potentially because of immature TWINKLE detachment from the DNA template. The stalling replisome induces DNA breaks, which elicits the mtDNA replication stress response, with induced serine and glutathione biosynthesis promoting dNTP synthesis.

(F) Model of the pathogenic consequences of the recessive TWINKLE mutation underlying IOSCA and infantile encephalohepatopathy. The mutation disturbs coupling of NTP binding and ssDNA, leading to NTP hydrolysis by TWINKLE without bound ssDNA. NTP hydrolysis without DNA binding depletes cells of dNTPs, resulting in mtDNA depletion specifically in post-mitotic tissues, with a low dNTP pool mostly serving mtDNA maintenance.

All data are presented as mean, and error bars indicate SEM. *p < 0.05, **p < 0.01, ***p < 0.001, **** < 0.0001. See also Figure S5.

respiratory chain-deficient muscle fibers of Deletor mice, was not induced in IOSCA mice (Figure S4E). These results show that IOSCA mice manifest a mitochondrial epileptic encephalohepatopathy replicating the key findings of IOSCA patients.

IOSCA mouse muscle showed significant but opposite metabolite findings compared with Deletors, including low amino acid levels (Figure 5A). Furthermore, IOSCA mouse muscle showed a dNTP pool imbalance with generally decreased concentrations of all dNTPs (Figure 5B). The findings in the Deletor and IOSCA mouse muscles suggest that TWINKLE-associated mtDNA maintenance disorders have genotype-specific effects on dNTP pools and that these changes contribute to the mtDNA findings in the disease: multiple mtDNA mutations in MM and mtDNA depletion in IOSCA.

Homology Modeling of Human TWINKLE with Mutations Causing IOSCA and MM

To understand the mechanism of how different TWINKLE mutations have opposite effects on dNTP pools, we performed homology modeling. We utilized the structure and analysis of a close TWINKLE homolog, T7 gene 4 ring helicase, with its subunits trapped in different catalytic steps (PDB ID 1E0J) (Figure 5C; Liao et al., 2005; Singleton et al., 2000). The T7 structure proposed that single-stranded DNA (ssDNA) is bound to only

one subunit in the hexamer at a time and, therefore, that the catalytic events of the helicase are sequential: NTP binding triggers ssDNA binding via specific loops of the same subunit, structural changes caused by the bound ssDNA initiate NTP hydrolysis, and DNA-binding loops move and translocate the ssDNA through the central pore of the helicase as proposed for the T7 helicase. The sequential mode and cooperation of the different subunits within the helicase ring rely on ssDNA binding, NTP hydrolysis, and the structure of the NTP binding site, which locates on the interface between two neighboring subunits, but only one of these subunits provides the main contacts for nucleotide binding (Singleton et al., 2000). NTP hydrolysis and ssDNA translocation by one subunit are accompanied by structural rearrangements in the NTP binding site as well as rotation of the subunit in the plane of the ring, which initiate the same sequence of catalytic events in the neighboring subunit. Without bound ssDNA, a hexamer can hydrolyze NTPs non-sequentially and is therefore very slow because of the lack of bound ssDNA propagation of the structural changes around the helicase ring (Crampton et al., 2006; Liao et al., 2005).

We mapped the IOSCA mutation on the attained TWINKLE helicase structure model and performed a comparative analysis of the corresponding part of the structure in T7 gene 4 ring helicase. The analysis predicted that the Y508C mutation affects the coupling between NTP hydrolysis and ssDNA binding/translocation, resulting in ssDNA-independent NTP hydrolysis (Figure 5D). Therefore, IOSCA mutation switches TWINKLE to the idling mode when NTP is hydrolyzed without DNA binding or unwinding. These results are consistent with previous findings of an increased NTP hydrolysis rate of recombinant IOSCA-TWINKLE protein (Hakonen et al., 2008), mtDNA depletion in IOSCA patients, as well as decreased dNTP pools identified in IOSCA mouse muscle.

The 13-amino-acid TWINKLE duplication, present in Deletor mice and in PEO patients, locates in the linker between the C-terminal helicase and N-terminal domain. This dominant mutation, coexisting in MM with WT subunits, extends the linker but does not affect the interaction between the subunits (Figure S5A). We predict that, upon MM mutation, the strain created on the subunit interface upon its rotation during catalysis leads to progressive accumulation of physical tension within the hexamer upon consecutive DNA unwinding cycles and induces the helicase to detach from the template, causing mtDNA replication stress and fork stalling, as has been shown to occur in Deletor muscle (Goffart et al., 2009).

These modeling data propose that IOSCA TWINKLE binds to DNA relatively rarely because NTP hydrolysis is ssDNA-independent in the mutant, but when the binding occurs, the mutant helicase will complete unwinding of the entire molecule. This might explain mtDNA depletion without deletions in affected tissues of IOSCA patients and in the mouse model. Furthermore, the continuous hydrolysis of NTP is likely to affect mitochondrial dNTP pools.

IOSCA and MM/PEO Patients Show Signs of 1C Metabolic Remodeling

To clarify whether a 1C imbalance also occurs in human patients, we were able to obtain blood and muscle from MM patients and blood from IOSCA patients with matched controls and performed a 100-metabolite analysis. Both patient groups showed genotype-specific metabolite fingerprints (Figure 6A) and shared metabolite patterns with the mice. Cystathionine, serine, and glutamic acid were among the eight metabolites changed significantly in all patient samples (Figures 6B–6F), and the main end products of transsulfuration, glutathione and taurine, were decreased in IOSCA blood (Figure 6B). IOSCA patients showed evidence of disturbed GAA/creatine metabolism (creatine:creatinine ratio fold change [FC] +2.9, $p = 0.008$) (Figure S6A). Of the purine metabolites, adenosine was decreased 7.6-fold in IOSCA compared with controls ($p = 0.03$). In PEO blood, intermediates of purine synthesis and catabolism (xanthine FC +1.5, $p = 0.0009$; inosine monophosphate [IMP] FC +1.4, $p = 0.012$; xanthosine FC +1.5, $p = 0.017$) as well as the alternative 1C donors betaine (FC +1.5, $p = 0.001$) and dimethylglycine (FC +1.6, $p = 0.002$) were changed significantly. These changes supported aberrations of transsulfuration and purine metabolism in both patient groups and creatine synthesis in IOSCA. Specific for the PEO patient muscle, acylcarnitines were increased, which suggested decreased utilization of fatty acids and accumulation of toxic fatty acid intermediates (Figure 6E).

DISCUSSION

The outstanding question in the mitochondrial disease field is what underlies the wide spectrum of disease manifestations. We designed mouse models for mitochondrial myopathy and IOSCA, both caused by TWINKLE helicase defects, to shed light on the physiological basis of tissue specificity. First, we report here that IOSCA knockin mice replicate the key manifestations of the human recessive IOSCA and Alpers-Huttenlocher syndromes, making these mice the first model for a common manifestation of mitochondrial disease in early childhood: epileptic encephalohepatopathy. Second, we report that primary mtDNA replication disorders modify the cellular serine-glycine-1C metabolism and dNTP pools. Figure 6G summarizes the main metabolic findings in the different tissues of our mice and patients, with major changes in the folate cycle-dependent biosynthetic pathways in the affected tissues.

Our protein modeling proposes that the mechanism in IOSCA involves active NTP hydrolysis by the mutant helicase, whereas, in the case of MM, replication stalling boosts dNTP synthesis. MM defects direct glucose carbons to serine de novo biosynthesis as well as glutathione synthesis, an antioxidant and reductant that, through the glutaredoxin system, also promotes dNTP synthesis (Sengupta and Holmgren, 2014). This explains why TWINKLE disorders mimic those of primary dNTP pool defects, including diseases caused by ribonucleotide reductase mutations. Severe protein defects result in a lack of dNTPs and consequent mtDNA depletion, whereas adult-manifesting defects involve metabolic remodeling of cellular biosynthesis pathways, the stalled replisome boosting nucleotide synthesis, resulting in aberrant dNTP pools and mtDNA deletion mutagenesis. These changes are limited to affected tissues and cell-autonomous, implying a relevance of our findings to primary and secondary conditions with mtDNA mutagenesis.

The finding of in vivo glucose carbon flux in the affected tissues of MM to serine and glutathione was unexpected. Serine

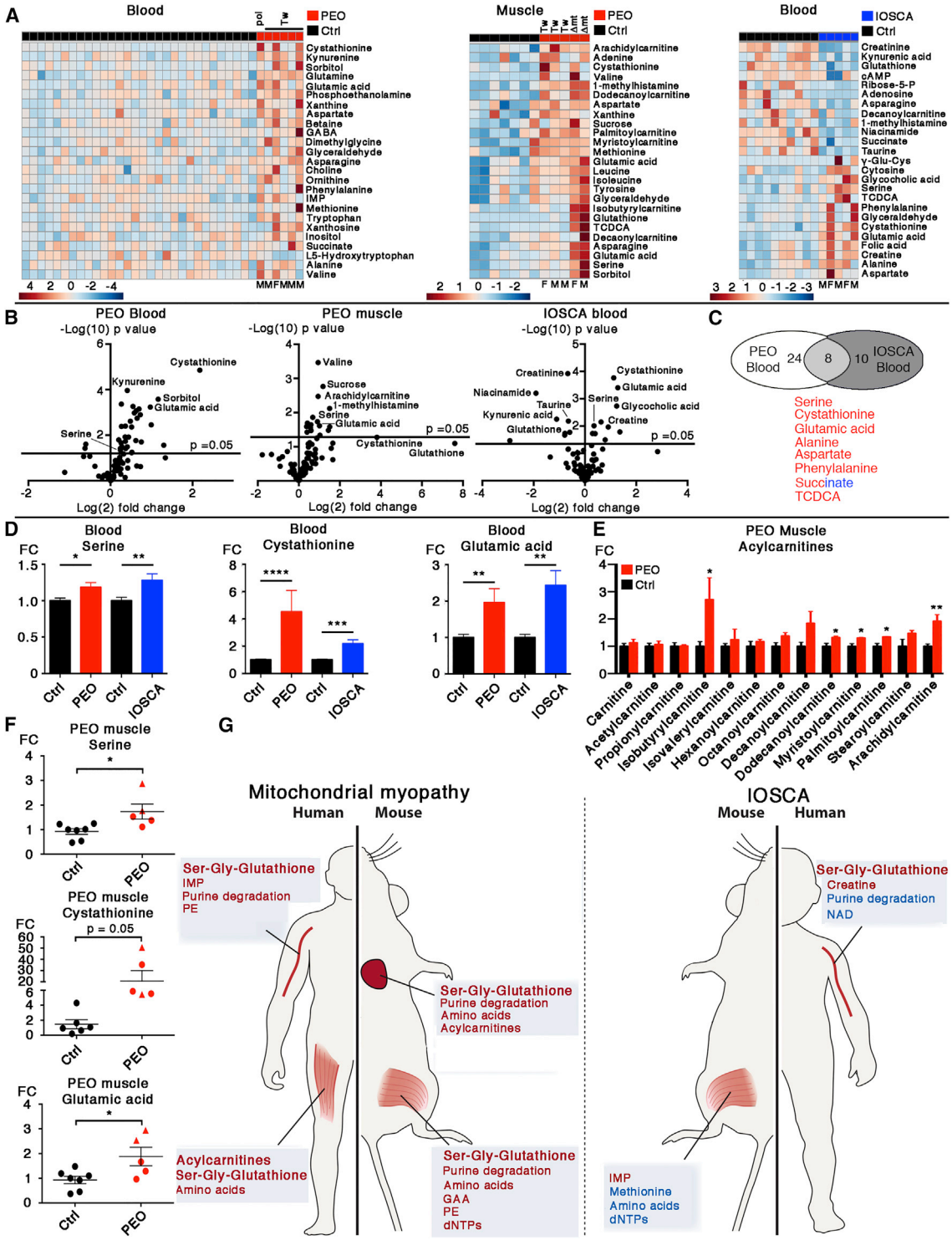

Figure 6. Human Patients with Mitochondrial Myopathy/PEO and IOSCA Show Steady-State Metabolomics Consistent with Increased Serine and Transsulfuration Metabolites

(A) Heatmaps of the top 25 most significantly changed metabolites in blood and muscle of patients with PEO (mitochondrial myopathy) and blood of IOSCA patients. The order of metabolites is based on hierarchical clustering. The scale bar indicates *Z* scores. Blood: 6 PEO patients; TWINKLE-PEO (Tw), n = 5; POLG-PEO (pol), n = 1; age- and gender-matched controls, n = 30; IOSCA patients, n = 5; their age and gender-matched controls (Ctrl), n = 10. Skeletal muscle, PEO patients: TWINKLE-PEO, n = 3; sporadic mtDNA deletion-associated PEO (Δmt), n = 2; controls, n = 7. Below the heatmaps, genders are indicated: M, male; F, female.

(B) Volcano plots of metabolites (samples as in A).

(legend continued on next page)

is a non-essential amino acid with multiple crucial roles in cellular metabolism. Its de novo synthesis from glucose is a three-step pathway, deviating a fraction of 3-phosphoglycerate from glycolysis toward serine. However, the role of de novo serine synthesis is not fully understood. We studied the evolutionary history of the rate-limiting enzyme PHGDH and show evidence that PHGDH coevolved with the transsulfuration enzymes CTH and CBS, suggesting that serine de novo synthesis is preserved to support cellular transsulfuration and glutathione synthesis. Recent data have suggested that de novo serine and glutathione synthesis are required for cancer cell proliferation to support the high demand of dNTP synthesis. Downregulation of this pathway has been found to decrease cellular dNTP pools (DeNicola et al., 2015; Mehrmohamadi et al., 2014). Ribonucleotide reductase utilizes nucleotide precursors, thioredoxin, and active glutaredoxin, which requires glutathione as a hydrogen donor (Sengupta and Holmgren, 2014). These components were induced in the affected tissues of Deletor mice, strongly supporting the conclusion that TWINKLE dysfunction in mitochondrial myopathy induces serine-directed glutathione synthesis to promote dNTP synthesis, a pathway showing strong conservation in species. Our finding suggests that PHGDH also has the potential to divert intracellular glucose flux toward serine in post-mitotic tissues (Locasale et al., 2011). We propose that serine de novo biosynthesis is a rapid response in skeletal muscle and heart to cellular metabolic/DNA stress, driving glutathione synthesis to prevent damage and support repair.

In yeast, ribonucleotide reductase determines genomic DNA replication fork speed by modulating dNTP pools, and chromosomal DNA damage induces dNTP synthesis (Poli et al., 2012). In Deletor mice, TWINKLE dysfunction causes mtDNA replication fork stalling (Goffart et al., 2009), which could also lead to decreased utilization of dNTPs. However, a stalled fork is a strong inducer of the DNA damage response when it occurs in genomic DNA. Our evidence of an increased dNTP synthesis pathway upon TWINKLE dysfunction suggests the existence of an mtDNA repair response, mimicking that of the nuclear genome. The response was, however, mutation-specific. The IOSCA mutation, not resulting in mtDNA replication stalling (Hakonen et al., 2008), did not induce serine/glutathione biosynthesis but had low dNTP pools. Our results show that TWINKLE mutations modify dNTP pools, which, together with the facts that TWINKLE is a licensing factor for mtDNA replication (Tyynismaa et al., 2004) and utilizes dNTPs as its fuel (Hingorani and Patel, 1996; Sawaya et al., 1999), suggests the intriguing possibility that TWINKLE activity synchronizes mtDNA replication with nutrient status and cellular anabolism.

Increased purine and glutathione synthesis could potentially form a carbon sink and increase homocysteine demand, thereby disturbing the methyl cycle. Indeed, we found accumulations of un-methylated precursors of creatine and phosphatidylcholine synthesis, the major users of 1C units in post-mitotic cells, in Deletor muscle. Of the total cellular methylation capacity, 60% is used for creatine synthesis, 30% for PC, and a minor part for protein, RNA, and DNA methylation (Mudd et al., 2007). Creatine synthesis and folate supply are especially important for the brain in childhood because inborn errors of creatine and folate metabolism manifest as ataxia and severe epilepsy (Stöckler et al., 1996). In adults, however, muscle is the primary site of creatine metabolism. It contains over 95% of body creatine, both synthesized on-site and imported (Balsom et al., 1994). This evidence suggests that the 1C dependence of post-mitotic cell types and tissues varies depending on their maturation state at a given age and time, making the infant brain and adult muscle especially susceptible to 1C metabolic aberrations, liver being the central organ metabolizing THF. Interestingly, a similar dichotomy in clinical manifestations—infantile onset brain/liver versus adult-onset muscle manifestations—is also typical for primary disorders of dNTP metabolism, caused by defects of ribonucleotide reductase 2B and purine-metabolic deoxyguanosine kinase (Bourdon et al., 2007; Mandel et al., 2001), suggesting that they share a similar pathogenic mechanism. We propose that the tissue specificity of mtDNA maintenance disorders, with severe mutations causing early-onset encephalohepatopathy and milder mutations adult-onset myopathy, is explained by the age-dependent susceptibility for folate-driven cytoplasmic biosynthesis pathways.

Concentrations of the distinct folate species are well below the saturation level of 1C-dependent biosynthetic enzymes (Scott and Weir, 1981; Suh et al., 2001), making the folate pool a metabolic rheostat. It matches nutrition availability and redox status with the biosynthetic requirements of a tissue in a context-dependent manner. The evidence suggests that a 1C metabolic defect and aberrant dNTP pools contribute to multiple mtDNA deletion formation, which occurs in mitochondrial disease, normal aging, and degenerative diseases such as Parkinson's disease neurons (Bender et al., 2006; Cortopassi et al., 1992). Indeed, folate supplementation has been reported to ameliorate disease-associated findings in fruit flies and patient cells carrying a mutation in *PINK1*, a gene underlying inherited Parkinson's disease (Tufi et al., 2014). In our study, short-term folinic acid supplementation for old Deletor mice was not sufficient to reverse their myopathy, which may be explained by their late-stage disease. However, the folate cycle is tightly regulated by vitamin cofactors and nutrients, offering multiple attractive targets for therapy tailored in a context- and manifestation time-dependent manner.

(C) Common metabolites changed in both PEO and IOSCA blood. Red text indicates an increased level in both patient groups. Succinate increased in PEO and decreased in IOSCA blood.

(D–F) Quantification of significantly changed metabolites in IOSCA and PEO blood (D) and PEO muscle (E and F). Red circles, TWINKLE-PEO; red triangles, single mtDNA deletion (PEO patients).

(G) Summary of the main metabolic findings in the different tissues of MM and IOSCA mouse models and human patients. Red, increased; blue, decreased. The size of the font reflects the prominence of the pathway in the specific tissue.

GABA, γ-aminobutyric acid; TCDCA, taurochenodeoxycholic acid; cAMP, cyclic AMP; ribose-5-P, ribose-5-phosphate; γ-Glu-Cys, γ-glutamylcysteine; NAD, nicotinamide adenine dinucleotide. All data are presented as mean, and error bars indicates SEM. *$p < 0.05$, **$p < 0.01$, ***$p < 0.001$, ****$p < 0.001$. See also Figure S6.

EXPERIMENTAL PROCEDURES

The human materials were collected and used with informed consent according to the Helsinki Declaration and approved by the Ethical Review Board of Helsinki University Central Hospital. The National Animal Experiment Review Board and Regional State Administrative Agency for Southern Finland approved our animal experiments, which were conducted according to the European Union Directive.

Patient Material and Sampling

The following PEO patient blood samples were used: males, n = 4; one female; all with a dominant duplication mutation (p.352–364) in *C10ORF2* (TWINKLE) (Suomalainen et al., 1992, 1997); one male patient carrying two recessive mutations in *POLG1* (patient II/11 in Luoma et al., 2004); ages, 38–56 years. The following muscle samples were used: samples from three TWINKLE PEO patients and two patients with single large mtDNA deletions. IOSCA patients were homozygous for recessive p.Y508C change (*C10ORF2)* in TWINKLE helicase (males, n = 3; females, n = 2; age, 31–41 years). Peripheral venous blood samples from the patients were used for metabolic analysis. PEO samples were taken with K_2-EDTA as an anticoagulant. Plasma was immediately separated, frozen, and stored at −140°C for metabolomic analyses. Serum was used for IOSCA patients.

Animal Models

Deletor mice expressed a dominant in-frame duplication homologous to our human patients' mutation (in mouse p.353-365) as reported previously. Two different transgene lines were used (Tyynismaa et al., 2005, 2010). Mice overexpressing wild-type TWINKLE showed no pathology (Tyynismaa et al., 2004). IOSCA mice were generated by introducing a c.1526 A > G mutation into *C10orf2* exon 3 by homologous recombination. The resulting mice were crossed with Flp recombinase-expressing C57BL/6 to remove the neomycin (NEO) cassette.

Folinic Acid Supplementation

Deletor mice were supplemented with PBS or 0.28 mg folinic acid (Sigma-Aldrich, catalog no. F7878) for eight weeks via intraperitoneal injections (first 5 consecutive days and continued twice a week until the end of the study) and via drinking water (0.28 mg/ml) throughout the study.

In Vivo [^{18}F]FDG Uptake and Positron Emission Tomography/Computed Tomography

The mice were given the glucose analog [^{18}F]FDG (5 MBq, > 76 MBq/nmol) intravenously and imaged for uptake with PET/CT (Inveon Multimodality, Siemens) under light anesthesia on temperature-controlled mats for a total of 1 hr. Standardized uptake values of [^{18}F]FDG uptake in different tissues were calculated from regions of interest (Carimas visualization and analysis software [http://www.turkupetcentre.fi/carimas]).

dNTP Pool Measurement

Total nucleotides were extracted and analyzed as in Martí et al. (2012). Briefly, extracts or standards were added to a reaction mixture (40 mM Tris/HCl [pH 7.5], 10 mM $MgCl_2$, 5 mM dithiothreitol, 0.25 μM primed oligonucleotide, 0.75 μM ^{3}H-dTTP or ^{3}H-dATP, and 0.30 U Taq DNA polymerase in a total of 20 μl) and incubated at 48°C for 60 min. 15 μl of mixture was spotted onto DE-81 filter paper and dried. The filter papers were washed (three times with 5% Na_2HPO_4 and once with water and 95% ethanol). The radioactivity was quantified by a liquid scintillation counter. We performed three to six measurements for all individual samples.

Protein, RNA, and DNA

Immunoblotting was done using the antibodies listed in the Supplemental Experimental Procedures. The mtDNA integrity and amount were analyzed by qRT-PCR as in Khan et al. (2014). mRNA levels were quantified by qRT-PCR (see Supplemental Experimental Procedures for primers used).

[U-^{13}C]-Glucose Flux Analysis

20 mg of [U-^{13}C]-glucose (Cambridge Isotope Laboratories, catalog no. CLM-1396) was injected via the tail vein into Deletor mice and WT littermates. Tissues were collected at 15 min, and the samples were analyzed by targeted selected reaction monitoring (SRM) liquid chromatography-tandem mass spectrometry [LC-MS/MS] on an Agilent 6460 QQQ instrument.

Statistical Methods

For statistical significance analysis we used unpaired Student's t test unless mentioned otherwise (see Supplemental Experimental Procedures). For outlier analysis we used the GraphPad Prism 6.0 robust regression and outlier removal (ROUT) method (Q = 1%). For false positive analysis in metabolomics we used the Benjamini-Hochberg method with a critical value of 0.2.

Metabolomics Analyses

Metabolomic and folate intermediate analyses were performed using Waters Acquity ultra performance liquid chromatography (UPLC) and triple-quadrupole mass spectrometry analysis. Formate was measured by gas chromatography (GC) MS analysis.

TWINKLE Homology Modeling and Structure Analysis

Homology modeling of the human TWINKLE hexamer was made using the structure of bacteriophage T7 gene 4 helicase-primase with a bound NTP analog (PDB ID 1E0J) (Singleton et al., 2000). For the sequences of the TWINKLE homologs we used the UniProt database (http://www.uniprot.org), and for alignment we used PROMALS3D (http://prodata.swmed.edu/promals3d/promals3d.php). For multiple sequence alignment and structure modeling we used the SWISS-MODEL server (http://www.swissmodel.expasy.org) (Arnold et al., 2006). The resulting model was analyzed in Accelrys Discovery Studio v4.1 (https://www.csc.fi).

SUPPLEMENTAL INFORMATION

Supplemental Information includes Supplemental Experimental Procedures, six figures, three tables, and one movie and can be found with this article online at http://dx.doi.org/10.1016/j.cmet.2016.01.019.

AUTHOR CONTRIBUTIONS

J.N. conceived the main experimental design and performance, analyzed data, and wrote the manuscript. I.P. performed IOSCA mouse generation and phenotype analyses. S.F., R.A.K., L.W., D.C., J.V., P.M., H.L., M.T., S.P.-K., N.A.K., J.B., and S.A. designed and performed experiments and analyzed data. T.L., P.I., and A.P. collected and analyzed patient material. A. Sajantila, A.R., and D.K.N. supervised experiments and analyzed data. H.T. and B.J.B. contributed to IOSCA mouse generation. V.V. supervised metabolomic experiments and analyzed data. C.J.C. and L.E. designed, performed, and supervised experiments and wrote the manuscript. A. Suomalainen designed and supervised the project, participated in data analysis, and wrote the manuscript. All authors commented on the manuscript.

ACKNOWLEDGMENTS

The authors wish to thank Anna Hakonen and Ksenia Sevastianova for patient sampling; Anu Harju, Markus Innilä, and Tuula Manninen for technical assistance; Johanna Silvola for technical help with PET imaging and data analysis; and Meri Kokkonen and Jatin Nandania for technical help with metabolomics analyses. The following funding resources are acknowledged: European Research Council, Academy of Finland, Sigrid Juselius Foundation, Jane and Aatos Erkko Foundation, University of Helsinki and Helsinki University Central Hospital (A.S.), Helsinki Biomedical Graduate School (J.N. and S.F.), and NIH R01CA172667 (D.K.N.). The PET studies were conducted within the Finnish Centre of Excellence in Cardiovascular and Metabolic Disease supported by the Academy of Finland, the University of Turku, the Turku University Hospital, and Åbo Akademi University.

Received: September 10, 2015
Revised: December 7, 2015
Accepted: January 28, 2016
Published: February 25, 2016

REFERENCES

Arnold, K., Bordoli, L., Kopp, J., and Schwede, T. (2006). The SWISS-MODEL workspace: a web-based environment for protein structure homology modelling. Bioinformatics *22*, 195–201.

Balsom, P.D., Söderlund, K., and Ekblom, B. (1994). Creatine in humans with special reference to creatine supplementation. Sports Med. *18*, 268–280.

Bender, A., Krishnan, K.J., Morris, C.M., Taylor, G.A., Reeve, A.K., Perry, R.H., Jaros, E., Hersheson, J.S., Betts, J., Klopstock, T., et al. (2006). High levels of mitochondrial DNA deletions in substantia nigra neurons in aging and Parkinson disease. Nat. Genet. *38*, 515–517.

Bourdon, A., Minai, L., Serre, V., Jais, J.P., Sarzi, E., Aubert, S., Chrétien, D., de Lonlay, P., Paquis-Flucklinger, V., Arakawa, H., et al. (2007). Mutation of RRM2B, encoding p53-controlled ribonucleotide reductase (p53R2), causes severe mitochondrial DNA depletion. Nat. Genet. *39*, 776–780.

Christensen, K.E., and MacKenzie, R.E. (2006). Mitochondrial one-carbon metabolism is adapted to the specific needs of yeast, plants and mammals. BioEssays *28*, 595–605.

Cortopassi, G.A., Shibata, D., Soong, N.W., and Arnheim, N. (1992). A pattern of accumulation of a somatic deletion of mitochondrial DNA in aging human tissues. Proc. Natl. Acad. Sci. USA *89*, 7370–7374.

Crampton, D.J., Mukherjee, S., and Richardson, C.C. (2006). DNA-induced switch from independent to sequential dTTP hydrolysis in the bacteriophage T7 DNA helicase. Mol. Cell *21*, 165–174.

DeNicola, G.M., Chen, P.H., Mullarky, E., Sudderth, J.A., Hu, Z., Wu, D., Tang, H., Xie, Y., Asara, J.M., Huffman, K.E., et al. (2015). NRF2 regulates serine biosynthesis in non-small cell lung cancer. Nat. Genet. *47*, 1475–1481.

Di Pietro, E., Wang, X.L., and MacKenzie, R.E. (2004). The expression of mitochondrial methylenetetrahydrofolate dehydrogenase-cyclohydrolase supports a role in rapid cell growth. Biochim. Biophys. Acta *1674*, 78–84.

Field, M.S., Szebenyi, D.M., and Stover, P.J. (2006). Regulation of de novo purine biosynthesis by methenyltetrahydrofolate synthetase in neuroblastoma. J. Biol. Chem. *281*, 4215–4221.

Garcia-Diaz, B., Garone, C., Barca, E., Mojahed, H., Gutierrez, P., Pizzorno, G., Tanji, K., Arias-Mendoza, F., Quinzii, C.M., and Hirano, M. (2014). Deoxynucleoside stress exacerbates the phenotype of a mouse model of mitochondrial neurogastrointestinal encephalopathy. Brain *137*, 1337–1349.

García-Martínez, L.F., and Appling, D.R. (1993). Characterization of the folate-dependent mitochondrial oxidation of carbon 3 of serine. Biochemistry *32*, 4671–4676.

Goffart, S., Cooper, H.M., Tyynismaa, H., Wanrooij, S., Suomalainen, A., and Spelbrink, J.N. (2009). Twinkle mutations associated with autosomal dominant progressive external ophthalmoplegia lead to impaired helicase function and in vivo mtDNA replication stalling. Hum. Mol. Genet. *18*, 328–340.

Hakonen, A.H., Heiskanen, S., Juvonen, V., Lappalainen, I., Luoma, P.T., Rantamaki, M., Goethem, G.V., Lofgren, A., Hackman, P., Paetau, A., et al. (2005). Mitochondrial DNA polymerase W748S mutation: a common cause of autosomal recessive ataxia with ancient European origin. Am. J. Hum. Genet. *77*, 430–441.

Hakonen, A.H., Goffart, S., Marjavaara, S., Paetau, A., Cooper, H., Mattila, K., Lampinen, M., Sajantila, A., Lönnqvist, T., Spelbrink, J.N., and Suomalainen, A. (2008). Infantile-onset spinocerebellar ataxia and mitochondrial recessive ataxia syndrome are associated with neuronal complex I defect and mtDNA depletion. Hum. Mol. Genet. *17*, 3822–3835.

Hingorani, M.M., and Patel, S.S. (1996). Cooperative interactions of nucleotide ligands are linked to oligomerization and DNA binding in bacteriophage T7 gene 4 helicases. Biochemistry *35*, 2218–2228.

Jain, M., Nilsson, R., Sharma, S., Madhusudhan, N., Kitami, T., Souza, A.L., Kafri, R., Kirschner, M.W., Clish, C.B., and Mootha, V.K. (2012). Metabolite profiling identifies a key role for glycine in rapid cancer cell proliferation. Science *336*, 1040–1044.

Khan, N.A., Auranen, M., Paetau, I., Pirinen, E., Euro, L., Forsström, S., Pasila, L., Velagapudi, V., Carroll, C.J., Auwerx, J., and Suomalainen, A. (2014). Effective treatment of mitochondrial myopathy by nicotinamide riboside, a vitamin B3. EMBO Mol. Med. *6*, 721–731.

Korhonen, J.A., Pham, X.H., Pellegrini, M., and Falkenberg, M. (2004). Reconstitution of a minimal mtDNA replisome in vitro. EMBO J. *23*, 2423–2429.

Li, Y., Calvo, S.E., Gutman, R., Liu, J.S., and Mootha, V.K. (2014). Expansion of biological pathways based on evolutionary inference. Cell *158*, 213–225.

Liao, J.C., Jeong, Y.J., Kim, D.E., Patel, S.S., and Oster, G. (2005). Mechanochemistry of t7 DNA helicase. J. Mol. Biol. *350*, 452–475.

Locasale, J.W., Grassian, A.R., Melman, T., Lyssiotis, C.A., Mattaini, K.R., Bass, A.J., Heffron, G., Metallo, C.M., Muranen, T., Sharfi, H., et al. (2011). Phosphoglycerate dehydrogenase diverts glycolytic flux and contributes to oncogenesis. Nat. Genet. *43*, 869–874.

Lönnqvist, T., Paetau, A., Nikali, K., von Boguslawski, K., and Pihko, H. (1998). Infantile onset spinocerebellar ataxia with sensory neuropathy (IOSCA): neuropathological features. J. Neurol. Sci. *161*, 57–65.

Luoma, P., Melberg, A., Rinne, J.O., Kaukonen, J.A., Nupponen, N.N., Chalmers, R.M., Oldfors, A., Rautakorpi, I., Peltonen, L., Majamaa, K., et al. (2004). Parkinsonism, premature menopause, and mitochondrial DNA polymerase gamma mutations: clinical and molecular genetic study. Lancet *364*, 875–882.

Mandel, H., Szargel, R., Labay, V., Elpeleg, O., Saada, A., Shalata, A., Anbinder, Y., Berkowitz, D., Hartman, C., Barak, M., et al. (2001). The deoxyguanosine kinase gene is mutated in individuals with depleted hepatocerebral mitochondrial DNA. Nat. Genet. *29*, 337–341.

Martí, R., Dorado, B., and Hirano, M. (2012). Measurement of mitochondrial dNTP pools. Methods Mol. Biol. *837*, 135–148.

Mehrmohamadi, M., Liu, X., Shestov, A.A., and Locasale, J.W. (2014). Characterization of the usage of the serine metabolic network in human cancer. Cell Rep. *9*, 1507–1519.

Mudd, S.H., Brosnan, J.T., Brosnan, M.E., Jacobs, R.L., Stabler, S.P., Allen, R.H., Vance, D.E., and Wagner, C. (2007). Methyl balance and transmethylation fluxes in humans. Am. J. Clin. Nutr. *85*, 19–25.

Naviaux, R.K., Nyhan, W.L., Barshop, B.A., Poulton, J., Markusic, D., Karpinski, N.C., and Haas, R.H. (1999). Mitochondrial DNA polymerase gamma deficiency and mtDNA depletion in a child with Alpers' syndrome. Ann. Neurol. *45*, 54–58.

Nikali, K., Suomalainen, A., Saharinen, J., Kuokkanen, M., Spelbrink, J.N., Lönnqvist, T., and Peltonen, L. (2005). Infantile onset spinocerebellar ataxia is caused by recessive mutations in mitochondrial proteins Twinkle and Twinky. Hum. Mol. Genet. *14*, 2981–2990.

Nilsson, R., Jain, M., Madhusudhan, N., Sheppard, N.G., Strittmatter, L., Kampf, C., Huang, J., Asplund, A., and Mootha, V.K. (2014). Metabolic enzyme expression highlights a key role for MTHFD2 and the mitochondrial folate pathway in cancer. Nat. Commun. *5*, 3128.

Nunnari, J., and Suomalainen, A. (2012). Mitochondria: in sickness and in health. Cell *148*, 1145–1159.

Pagliarini, D.J., and Rutter, J. (2013). Hallmarks of a new era in mitochondrial biochemistry. Genes Dev. *27*, 2615–2627.

Pagliarini, D.J., Calvo, S.E., Chang, B., Sheth, S.A., Vafai, S.B., Ong, S.E., Walford, G.A., Sugiana, C., Boneh, A., Chen, W.K., et al. (2008). A mitochondrial protein compendium elucidates complex I disease biology. Cell *134*, 112–123.

Pike, S.T., Rajendra, R., Artzt, K., and Appling, D.R. (2010). Mitochondrial C1-tetrahydrofolate synthase (MTHFD1L) supports the flow of mitochondrial one-carbon units into the methyl cycle in embryos. J. Biol. Chem. *285*, 4612–4620.

Poli, J., Tsaponina, O., Crabbé, L., Keszthelyi, A., Pantesco, V., Chabes, A., Lengronne, A., and Pasero, P. (2012). dNTP pools determine fork progression and origin usage under replication stress. EMBO J. *31*, 883–894.

Sawaya, M.R., Guo, S., Tabor, S., Richardson, C.C., and Ellenberger, T. (1999). Crystal structure of the helicase domain from the replicative helicase-primase of bacteriophage T7. Cell *99*, 167–177.

Schirch, V., and Strong, W.B. (1989). Interaction of folylpolyglutamates with enzymes in one-carbon metabolism. Arch. Biochem. Biophys. *269*, 371–380.

Scott, J.M., and Weir, D.G. (1981). The methyl folate trap. A physiological response in man to prevent methyl group deficiency in kwashiorkor (methionine deficiency) and an explanation for folic-acid induced exacerbation of subacute combined degeneration in pernicious anaemia. Lancet *2*, 337–340.

Sengupta, R., and Holmgren, A. (2014). Thioredoxin and glutaredoxin-mediated redox regulation of ribonucleotide reductase. World J. Biol. Chem. *5*, 68–74.

Singleton, M.R., Sawaya, M.R., Ellenberger, T., and Wigley, D.B. (2000). Crystal structure of T7 gene 4 ring helicase indicates a mechanism for sequential hydrolysis of nucleotides. Cell *101*, 589–600.

Spelbrink, J.N., Li, F.Y., Tiranti, V., Nikali, K., Yuan, Q.P., Tariq, M., Wanrooij, S., Garrido, N., Comi, G., Morandi, L., et al. (2001). Human mitochondrial DNA deletions associated with mutations in the gene encoding Twinkle, a phage T7 gene 4-like protein localized in mitochondria. Nat. Genet. *28*, 223–231.

Stöckler, S., Isbrandt, D., Hanefeld, F., Schmidt, B., and von Figura, K. (1996). Guanidinoacetate methyltransferase deficiency: the first inborn error of creatine metabolism in man. Am. J. Hum. Genet. *58*, 914–922.

Strong, W.B., Tendler, S.J., Seither, R.L., Goldman, I.D., and Schirch, V. (1990). Purification and properties of serine hydroxymethyltransferase and C1-tetrahydrofolate synthase from L1210 cells. J. Biol. Chem. *265*, 12149–12155.

Suh, J.R., Herbig, A.K., and Stover, P.J. (2001). New perspectives on folate catabolism. Annu. Rev. Nutr. *21*, 255–282.

Suomalainen, A., Majander, A., Haltia, M., Somer, H., Lönnqvist, J., Savontaus, M.L., and Peltonen, L. (1992). Multiple deletions of mitochondrial DNA in several tissues of a patient with severe retarded depression and familial progressive external ophthalmoplegia. J. Clin. Invest. *90*, 61–66.

Suomalainen, A., Majander, A., Wallin, M., Setälä, K., Kontula, K., Leinonen, H., Salmi, T., Paetau, A., Haltia, M., Valanne, L., et al. (1997). Autosomal dominant progressive external ophthalmoplegia with multiple deletions of mtDNA: clinical, biochemical, and molecular genetic features of the 10q-linked disease. Neurology *48*, 1244–1253.

Tibbetts, A.S., and Appling, D.R. (2010). Compartmentalization of Mammalian folate-mediated one-carbon metabolism. Annu. Rev. Nutr. *30*, 57–81.

Tufi, R., Gandhi, S., de Castro, I.P., Lehmann, S., Angelova, P.R., Dinsdale, D., Deas, E., Plun-Favreau, H., Nicotera, P., Abramov, A.Y., et al. (2014). Enhancing nucleotide metabolism protects against mitochondrial dysfunction and neurodegeneration in a PINK1 model of Parkinson's disease. Nat. Cell Biol. *16*, 157–166.

Tyynismaa, H., Sembongi, H., Bokori-Brown, M., Granycome, C., Ashley, N., Poulton, J., Jalanko, A., Spelbrink, J.N., Holt, I.J., and Suomalainen, A. (2004). Twinkle helicase is essential for mtDNA maintenance and regulates mtDNA copy number. Hum. Mol. Genet. *13*, 3219–3227.

Tyynismaa, H., Mjosund, K.P., Wanrooij, S., Lappalainen, I., Ylikallio, E., Jalanko, A., Spelbrink, J.N., Paetau, A., and Suomalainen, A. (2005). Mutant mitochondrial helicase Twinkle causes multiple mtDNA deletions and a late-onset mitochondrial disease in mice. Proc. Natl. Acad. Sci. USA *102*, 17687–17692.

Tyynismaa, H., Carroll, C.J., Raimundo, N., Ahola-Erkkilä, S., Wenz, T., Ruhanen, H., Guse, K., Hemminki, A., Peltola-Mjøsund, K.E., Tulkki, V., et al. (2010). Mitochondrial myopathy induces a starvation-like response. Hum. Mol. Genet. *19*, 3948–3958.

Van Goethem, G., Luoma, P., Rantamäki, M., Al Memar, A., Kaakkola, S., Hackman, P., Krahe, R., Löfgren, A., Martin, J.J., De Jonghe, P., et al. (2004). POLG mutations in neurodegenerative disorders with ataxia but no muscle involvement. Neurology *63*, 1251–1257.

Zeviani, M., Servidei, S., Gellera, C., Bertini, E., DiMauro, S., and DiDonato, S. (1989). An autosomal dominant disorder with multiple deletions of mitochondrial DNA starting at the D-loop region. Nature *339*, 309–311.

Cell Metabolism, Volume *23*

Supplemental Information

Mitochondrial DNA Replication Defects Disturb Cellular dNTP Pools and Remodel One-Carbon Metabolism

Joni Nikkanen, Saara Forsström, Liliya Euro, Ilse Paetau, Rebecca A. Kohnz, Liya Wang, Dmitri Chilov, Jenni Viinamäki, Anne Roivainen, Päivi Marjamäki, Heidi Liljenbäck, Sofia Ahola, Jana Buzkova, Mügen Terzioglu, Nahid A. Khan, Sini Pirnes-Karhu, Anders Paetau, Tuula Lönnqvist, Antti Sajantila, Pirjo Isohanni, Henna Tyynismaa, Daniel K. Nomura, Brendan J. Battersby, Vidya Velagapudi, Christopher J. Carroll, and Anu Suomalainen

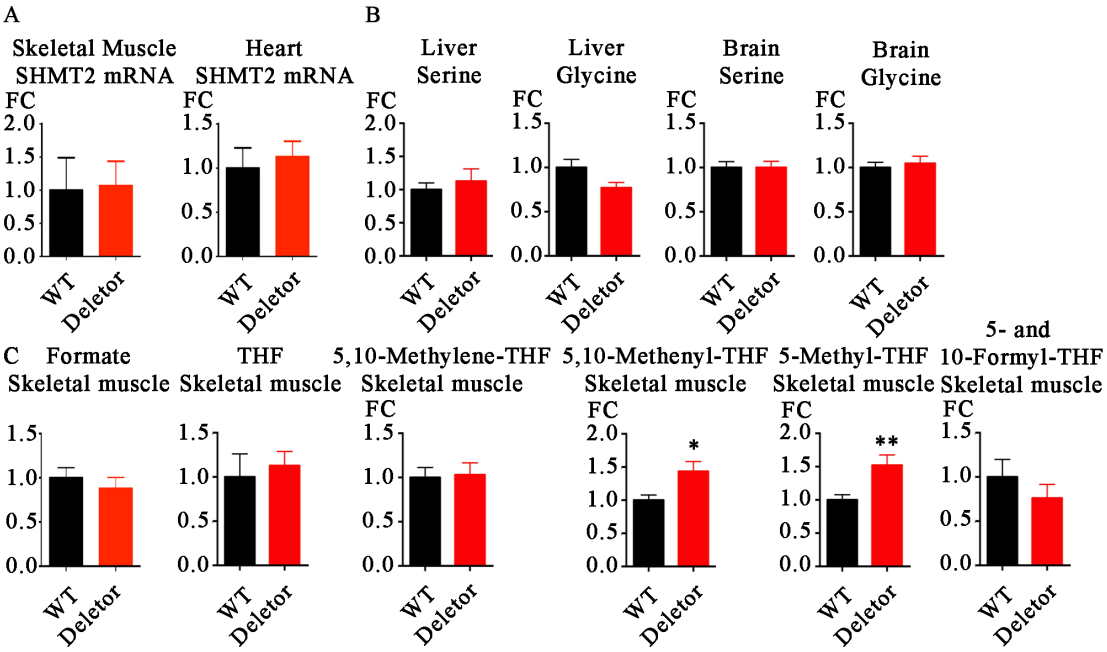

Figure S1. Related to Figure 1

(a) RNA expression of SHMT2 in skeletal muscle and heart.
(b) Levels of serine and glycine in Deletor liver and brain.
(c) Level of formate and folate intermediates in female mice. Formate: WT n=5, Deletor n=5; Folate intermediates: WT n=10, Deletor n=10;

All data in the figure are presented as mean and error bars indicate standard error of the mean. * $p < 0.05$, ** $p < 0.01$

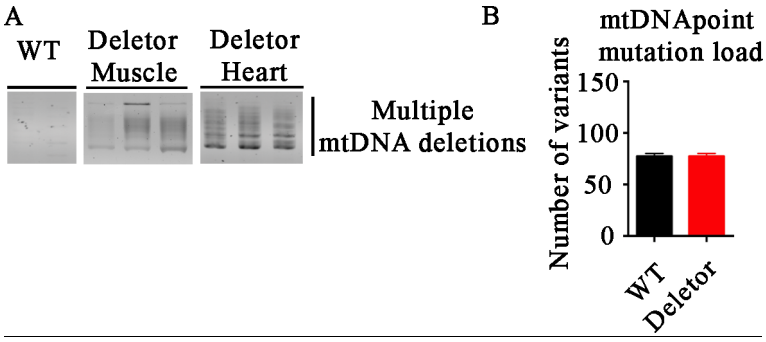

Figure S2. Related to Figure 2

(a) Multiple mtDNA deletions in Deletor skeletal muscle and heart, long-range PCR.
(b) mtDNA point mutation load in Deletor skeletal muscle. Deletor n=8, WT n=7.

All data in the figure are presented as mean and error bars indicate standard error of the mean.

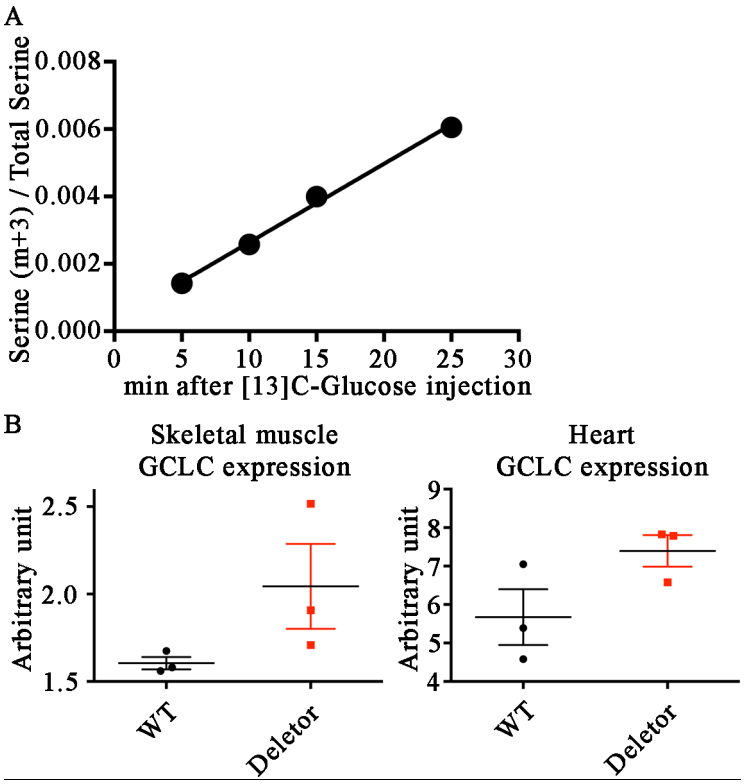

Figure S3. Related to Figure 3

(a) Level of m+3 serine in different time points in heart after [U-^{13}C]-glucose injection
(b) Western blot quantitation of GCLC in skeletal muscle and heart.

All data in the figure are presented as mean and error bars indicate standard error of the mean.

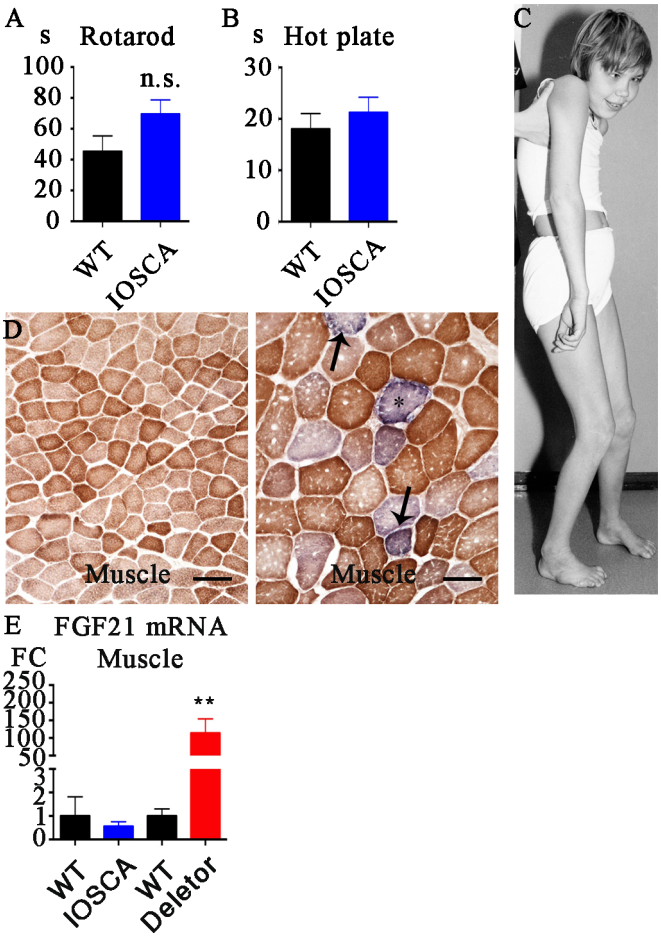

Figure S4. Related to Figure 4

(a) Rotarod test of IOSCA and WT mice.
(b) Hot plate test of IOSCA and WT mice.
(c) IOSCA patient
(d) Left panel: IOSCA patient skeletal muscle, normal cytochrome-c-oxidase (COX) activity (brown). Right panel: PEO patient skeletal muscle: numerous COX-negative (blue; arrows) or "ragged red" fibers (star).
(e) FGF21 mRNA expression in skeletal muscle of IOSCA and Deletor mice, QPCR.

All data in the figure are presented as mean and error bar indicates standard error of the mean. * $p < 0.05$, ** $p < 0.01$.

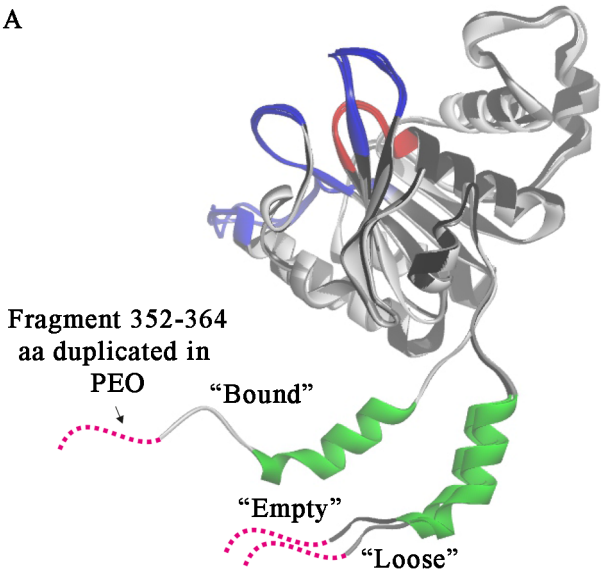

Figure S5. Related to Figure 5

(a) Helicase domains in three different catalytic states were superimposed to show the degree of each subunit rotation upon ssDNA translocation. Rotation generates tension on the intersubunit surface which is absorbed by the linker (350-384 aa) including fragment 352-364 duplicated in PEO. We propose that longer linker accumulates physical strain between subunits slowing down DNA unwinding and promoting premature dissociation from the replicative fork.

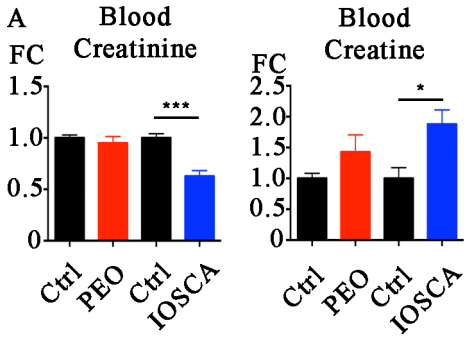

Figure S6. Related to Figure 6

(a) Level of creatinine and creatine in PEO and IOSCA patient blood.

All data in the figure are presented as mean and error bars indicate standard error of the mean. * $p < 0.05$, *** $p < 0.001$

Table S1 List of analyzed metabolites. Related to Figure 2.

Table S2 Changed metabolites in Deletor skeletal muscle. Related to Figure 2.

Metabolite name	Fold change	p-value
Glycine	1.68	0.002
Betaine	1.99	0.003
Homoserine	1.16	0.005
Serine	1.64	0.005
Leucine	1.51	0.008
Choline	2.06	0.01
Threonine	1.52	0.011
Proline	1.56	0.011
Creatine	1.31	0.016
Hypoxanthine	1.38	0.017
5-Hydroxyindole-3-acetic acid	1.81	0.018
Phenylalanine	1.53	0.019
Taurine	1.34	0.02
Guanidinoacetic Acid	1.39	0.021
Niacinamide (B3)	1.54	0.021
Methionine	1.51	0.022
Isoleucine	1.47	0.022
Phosphoethanolamine	1.7	0.025
Hydroxyproline	1.26	0.027
Creatinine	1.56	0.027
Glutamine	1.4	0.027
Aspartate	1.34	0.031
Glutathione (reduced)	1.35	0.033
Asparagine	1.32	0.037
Neopterin	1.2	0.037
Valine	1.42	0.038
Glutamic Acid	1.61	0.038
GABA	1.87	0.04
Glyceraldehyde	1.46	0.045
Alanine	1.29	0.049

Table S3 Changed metabolites in Deletor heart. Related to Figure 2.

Metabolite name	Fold change	p-value
Serine	1.98	0.00090
Glycine	1.56	0.00285
Uracil	1.33	0.00311
Betaine	3.28	0.00501
Inosine	1.52	0.00826
Xanthosine	2.71	0.00838
2-Aminoisobutyric acid	1.68	0.00933
Threonine	1.43	0.00982
Ornithine	1.63	0.01224
Proline	1.44	0.01270
Aspartate	1.43	0.01399
DimethylGlycine	2.32	0.01403
Cystathionine	2.81	0.01445
Stearoyl Carnitine	3.24	0.01699
5-Deoxy-5Methylthio	1.31	0.01786
Guanosine	2.20	0.01802
Trimethylamine-N-Oxide	1.68	0.02053
Tryptophan	1.21	0.03221
Palmitoyl Carnitine	2.86	0.03352
Aminodipic Acid	1.41	0.03372
Adenosine	3.17	0.03794
5-Hydroxyindole-3-acetic acid	2.46	0.03872
Creatine	0.88	0.03928
Isoleucine	1.33	0.04005
Valine	1.24	0.04696

Movie S1 Epileptic seizure of IOSCA mouse. Related to Figure 4.

Supplemental Experimental Procedures

Generation of IOSCA knock-in mice

The 8152 bp fragment of *C10orf2* (GeneID: 226153) including *Mrpl43* exons 1-3 was generated with PCR from R1-ES-cell (Sv129 strain) DNA, cloned in to pCR®-Blunt II-TOPO Vector, and verified by Sanger sequencing. The *C10orf2* fragment was subsequently cloned in to amp^R vector PL253 (http://ncifrederick.cancer.gov/research/brb/recombineeringinformation.aspx) carrying HSV-tk selection cassette (necessary for ES-cell selection). Reverse LoxP sequences were inserted into *C10orf2* introns 2 and 4, using recombineering technique. The selection of LoxP sites was based on low conservation of the intronic region, to avoid affecting non-coding regulatory sites (Ensembl database). The point mutation c.1526A>G resulting in a homologous p.Y509C substitution was introduced to exon 3. The final construct including two loxP sites, neo-cassette with flanking frt sequences, IOSCA mutation and HSV-tk selection cassette, was linearized with NotI and electroporated into Sv129 ES-cells. A total of 282 ES cell clones survived double selection. Clones were first screened with PCR using primers for the neo-cassette and for a region outside the targeted genomic area, and verified with Southern blot analysis. Two clones were selected for subsequent C57BL/6 blastocyst injections. Resulting chimeras were crossed with Flp recombinase expressing transgenic C57BL/6 strain (Takeuchi et al., 2002) (http://www.ncbi.nlm.nih.gov/pubmed/12051751), to remove the neo-cassette, and the successful removal was analyzed by PCR. The resulting mice, carrying IOSCA knock-in allele, were back-crossed to C57BL/6, utilizing a speed-congenics strategy, and whole-genome SNP genotyping as basis for selection of breeding pairs. Congenic strain of transgenic mice was obtained in sixth mouse generation.

Deletor mice

Male mice were used in most experiments but females were used in folinic acid supplementation and flux experiments.

Control mice

Our two different transgenic mouse models, IOSCA and Deletor, are in the same C57Bl6 background, but generated 10 years apart from each other. Their WT littermates are maintained separate in our lab, as controls for their specific disease model. The diseased mice and their controls were always sampled together, and handled and analyzed identically in parallel.

Metabolomics data analysis.

Metabolomics data analysis was carried out using a web-based comprehensive metabolomics data processing tool, MetaboAnalyst 3.0 (Xia et al., 2012; Xia et al., 2009). Non-transformed and autoscaled data i.e., mean-centered and divided by the standard deviation of each variable, was used for various data analyses. To analyze differences among groups, univariate analyses, Ttest2 and ANOVA were used. Separation among groups was tested by unsupervised multivariate analysis, principal component analysis (PCA).

MtDNA point mutation analysis

Quantification of mtDNA point mutations was performed using a next-generation sequencing method. MtDNA was amplified from muscle DNA using REPLI-g Mitochondrial DNA kit (Qiagen). Illumina compatible sequencing libraries were generated with Nextera DNA sample preparation kit (Illumina, San Diego, CA, USA) and sequenced with an Illumina HiSeq system.

Western blotting

Total protein was extracted with 1 % Triton-X in PBS. Proteins were separated by SDS-PAGE using 4-20 % gradient gels and transferred to PVDF membranes. Blots were blocked with 5 % milk in Tris-buffered saline with Tween 20 (TBST) buffer for 1 hour and antibodies were incubated at 4ºC overnight at 1:1000 dilution in 1 % milk in TBST buffer. Antibodies used for Western analyses were: MTHFD2 (Abcam, #ab37840), MTHFD1L (Proteintech, 16113-1-AP), CTH/CSE (Proteintech, 12217-1-AP), GCLC (Proteintech, 12601-1-AP), SDHA (Abcam, ab14715), and B-ACTIN (Santa Cruz, sc1616).

Glutathione peroxidase and reductase activity assays

Glutathione peroxidase activity was measured as described in (Brigelius-Flohe et al., 2002). Briefly, a frozen tissue sample was placed to a buffer containing 100 mM Tris-HCl, pH 7.6, 300 mM NaCl, 0.01 % Triton-X100 and protease inhibitors (30 mg of tissue per 1ml of buffer) and homogenized in

Precellys bead homogenizer. Lysate was centrifuged at 14000 rpm for 20 min, at +4°C and supernatant was collected. Enzyme activity was analyzed in duplicates for each sample using 96-well plate at 43°C. Single reaction mixture contained 10 µL of sample, 190 µL of assay buffer (100 mM Tris-HCl, pH7.6; 5 mM EDTA; 1 mM sodium azide; 3 mM glutathione (GSH); 0.2 mM NADPH; 0.1 % Triton-X100; 600 mU of glutathione reductase from type III baker's yeast (Sigma). Reaction was started by 10 µL of 1mM H_2O_2 to final concentration of 50 µM. Kinetics of NADPH consumption was measured at 340 nm for 2 min with 0.09 min intervals using SpectraMax plate reader (Molecular devices). Glutathione reductase activity in the same lysate was measured in duplicates using 96-well plate at room temperature. The reaction mixture contained 10 µL of sample, 150 µL of 100 mM potassium phosphate buffer, pH 7.0; 1 mM EDTA; 0.03 mg/ml DTNB. Reaction was initiated by addition of 50 µL of 0.16 mg/ml NADPH. Kinetics of TNB accumulation was monitored at 412 nm for 5 min with 30 s intervals between measurements.

Mouse tissue sampling, histology, histochemistry

The animals were euthanized at the age of 22-27 months (MM-mice) or 19-27 months (IOSCA mice). The time was determined by aging (Deletor) and symptoms (IOSCA) of the mice. The tissues were extracted, snap-frozen in liquid nitrogen and stored at -80°C until metabolomic analysis. For histochemistry of cytochrome c oxidase and succinate dehydrogenase activities, muscle samples were embedded in Tissue-Tek O.C.T.™ Compound (Sakura # 4583) and frozen in isopentane, cooled with liquid nitrogen. Brain samples were prepared with a mold filled with Tissue-Tek O.C.T.™ compound and frozen at -80ºC. Formalin-fixed paraffin-embedded tissues were processed as previously described in (Ahola-Erkkila et al., 2010). Blood samples were collected by heart puncture and incubated for 15 min at RT. After centrifugation at 3000g at +4°C for 15 minutes serum was collected and stored at -80 °C for metabolomics analyses. COX/SDH histochemical activity analyses were performed as previously described (Ahola-Erkkila et al., 2010).

***In vivo* [^{18}F]-fluorodeoxyglucose [^{18}F]-FDG uptake, positron emission/computer tomography**

Food was removed from the mouse cages four hours before [^{18}F]-FDG uptake assay. The mice were anesthetized with isoflurane inhalation and intravenous catheter was installed to tail vein 15 minutes before intravenous injection of glucose analogue [^{18}F]-FDG (5 MBq, >76 MBq/nmol). During PET/CT (Inveon Multimodality, Siemens), the mice remained under light anesthesia on temperature-controlled mats for a total of one hour.

dNTP pool measurement

dNTP pools are known to show remarkable asymmetry, variability, cell-type and -cycle specificity (Gandhi and Samuels, 2011; Traut, 1994), and the pools in postmitotic cells are 100-1000 fold lower than in cycling cells (Khrishnan et al. JBC 2014). Our disease models and their specific littermate controls were sampled together, and handled and analyzed identically in parallel, and we used for the dNTP analysis the sensitive polymerase-based assay (Marti et al., 2012). Tissues were homogenized in 10 volumes (v/w) of buffer containing 10 mM Tris/HCl, pH 7.5, 0.2 mM ethylene glycol tetra-acetic acid (EGTA), 0.5 % bovine serum albumin (BSA), 210 mM mannitol and 70 mM sucrose, using polytron homogenizer. The tissue homogenate was centrifuged at 1000 x g for 10 min at 4°C. Cold methanol (-20°C) was added to the supernatants to a final concentration of 60% (v/v). After 3 hours at -80°C the samples were heated at 95°C for 3 min, cooled down on ice and then centrifuged at 16 000 x g for 20 min at 4°C. The supernatants were transferred to new tubes and dried. The pellets were dissolved in cold water and stored at -80°C until further analysis. The total dNTP pools were determined essentially as described in (Marti et al., 2012). Briefly, appropriate amount of extracts or standards were added to a reaction mixture containing 40 mM Tris/HCl, pH 7.5, 10 mM $MgCl_2$, 5 mM dithiothreitol (DTT), 0.25 µM specific primed oligonucleotide, 0.75 µM ^{3}H-dTTP or ^{3}H-dATP, 0.30 unit Taq DNA polymerase in a total of 20 μl. The reaction mixtures were incubated at 48°C for 60 min, and then 15 μl of the reaction mixture were spotted onto DE-81 filter paper, and dried. The filter papers were washed three times with 5% Na_2HPO_4, once with water and once with 95% ethanol. The reaction products were quantified by liquid scintillation counting. Three to six measurements were performed for all individual samples.

mRNA analyses

Total RNA was extracted from mouse tissues using Trizol reagent (Life Technologies, #15596-026) and a bead homogenizer (Precellys, Bertin Technologies). Two µg of RNA was DNase treated (Turbo DNAse; Life Technologies, #AM2238), of which 1 µg was used for cDNA synthesis (Maxima First Strand cDNA synthesis kit, Thermo Scientific, #K1672) and 1 µg for negative control reaction with no

reverse transcriptase. The PCR conditions were optimized to produce one specific product, and quantitative PCR was performed using iQ Sybr Green (Biorad, #172-5006) on a CFX96 Touch Real-Time PCR System (BioRad). For *Fgf21* amplification 5 µl of cDNA was used, and 0.5 µl for all other genes. Relative expression of a transcript was determined by normalizing to the expression of house-keeping genes beta-actin and 18S rRNA, and calculated using the ddCT method. The following primers were used for mRNA quantitation.
FGF21: 5'-CTGGGGGTCTACCAAGCATA-3', 5'-CACCCAGGATTTGAATGACC-3'; ACTB: 5'-ATGCTCCCCGGGCTGTAT-3', 5'-CATAGGAGTCCTTCTGACCCATTC-3'; rRNA18S: 5'-CGGACAGGATTGACAGATTG-3', 5'-CAAATCGCTCCACCAACTAA-3'; MTHFD2: 5'-AGGTCCCAAGCCTTTGAGTT-3', 5'-GTAAGGGAGTGCCGTTGAAA-3'; PSAT1: 5'-AGTGGAGCGCCAGAATAGAA-3', 5'-CTTCGGTTGTGACAGCGTTA-3'; PHGDH: 5'-GACCCCATCATCTCTCCTGA-3', 5'-GCACACCTTTCTTGCACTGA-3'

Formate analysis
The tissue samples were weighed and water added to achieve a total weight of 0.5 g. The samples were mechanically homogenized with OMNI TH220 tissue homogenizer, and 25 µl of internal standard (1 mg/mL of aqueous deuterated formic acid) was added. Acetonitrile (1.5 mL) was gradually added while simultaneously vortexing the sample; the sample was mixed for an additional 1 min and centrifuged. The top layer was transferred into a new tube, and acetonitrile was evaporated under a gentle stream of nitrogen at 40°C. The aqueous residue was transferred into a 20-mL headspace vial, and 250 mg of anhydrous sodium sulfate was mixed into the solution to obtain salting-out. 50 µL of 5M sodium hydroxide solution, 50 µL of 0.1 M tetrabutylammonium hydrogen sulfate (TBA-HSO4), and 50 µL of dimethyl sulfate (DMS) were added and mixed.
Gas chromatography (GC)– mass spectrometry (MS) analysis was performed as in (Rasanen et al., 2010) with cryogenic cooling with carbon dioxide. The GC was used in the split-less mode with a constant column flow of 2 mL/min. The injector port temperature was 200°C, and transfer line temperature 280°C. The oven temperature was initially 0°C for 2 min and then increased by 15°C/min to 250°C. The mass detector was operated in electron-ionization and selected ion monitoring mode. To enhance the sensitivity of the method, only ions with m/z 31, 32, 60, and 61 were monitored. These ions were also used as target and qualifier ions for the quantification. The ITEX parameters were as in (Rasanen et al., 2010).

Metabolomics analysis

Chemicals and reagents. All the metabolite standards, ammonium formate, ammonium acetate, ammonium hydroxide, β-mercaptoethanol, ascorbic acid, potassium hydroxide and HEPES buffer were from Sigma-Aldrich. Folic acid, tetrahydrofolic acid (THF), 5-methyl-, 5-formyl-, 5,10-methenyl- and 5,10-methylene-THF were from Schricks Laboratory, Switzerland. Rat plasma (Innovative Research Laboratory, USA) containing endogenous folate polyglutamates deconjugase was incubated with activated charcoal (750mg/15ml) for 90 min at +4 °C, centrifuged and stored at -20 °C until use. Formic acid (FA), 2-proponol, acetonitrile (ACN), and methanol: all HiPerSolv CHROMANORM, HPLC grade, BDH prolabo. Isotope-labeled internal standards: Cambridge Isotope Laboratory. Inc., USA. Deionized milliQ water was purified up to a resistivity of 18 MΩ (Barnstead EASYpure RoDi ultrapure water purification system, Thermo scientific, Ohio, USA).

Metabolite extraction protocol. For 100 metabolite analysis, calibration solutions were prepared in 96-well plate by serial dilution of the stock calibration mix using Hamilton's MICROLAB® STAR line (Hamilton, Bonaduz AG, Switzerland) liquid handling robot system. Starting from a stock solution mix, 10 additional lower working solutions were prepared using water as the diluent to build the calibration curves. For folate intermediate analysis, 12 additional lower working standard solutions were prepared using 50 mM HEPES buffer, 1% ascorbic acid, 1% β-mercaptoethanol, pH 8.0, as diluent, to build the calibration curves.

Tissue samples. For 100 metabolites analysis, frozen tissue samples (muscle, heart, liver, and brain; 15 – 35 mg) were homogenized by Precellys-24 bead homogenizer (1.4 mm beads) with 20 µl of labeled internal standard mix and extraction solvent (1:30, sample:solvent), in a two-step extraction process. First, 15 parts of precooled 100% ACN + 1% FA was added to the sample and homogenized for three cycles, 20 s each, at 5,500 rpm; 30 s pause between each homogenization interval. After homogenization, the sample tubes were centrifuged for 10 min, 5000 rpm, 4^{o} C in an Eppendorf 5404R centrifuge and the supernatant was collected. In the second step, 15 parts of 80/20% ACN/H_2O + 1%

FA was added to the remaining pellet, steps repeated as above, pooled with the first extract, and centrifuged for 15 min, 5000 rpm, 4^{o} C.

Serum samples. For 100 metabolite analysis, 10 µL of labeled internal standard mixture was added to 100 µL of serum sample. Metabolites were extracted with 1:4 (sample:solvent) of 100% ACN + 1% FA solvent.
The collected extracts were dispensed in OstroTM 96-well plate (Waters Corporation, Milford, USA) and filtered by applying vacuum at a delta pressure of 300-400 mbar for 2.5 min on robot's vacuum station. The clean extract was collected to a 96-well collection plate, placed under OstroTM plate. The collection plate was sealed and centrifuged for 15 min, 5000 rpm, 4^{o} C and placed in auto-sampler of the liquid chromatography system for the injection.
For folate intermediate analysis, frozen tissue samples (muscle 40-50 mg) were homogenized in Precellys bead homogenizer in 400 µL of extraction buffer (50mM HEPES with 1% ascorbic acid and 1% B-mercaptoethanol, pH 8.0), for three cycles of 30 s each, 5,500 rpm, with 30 s pause between each homogenization interval. 40 µL of charcoal treated rat plasma was added, and the homogenate was incubated at 37 ºC for 3 hrs for folate deconjugation, followed by centrifugation at 14000 rpm, 15 min at 4°C. 300 µL of the supernatant was centrifuged through 10 kDa cut-off filters (sigma Aldrich, Finland) at 14000 rpm, 30 min at 4°C, and filtrate was collected for injection into the chromatographic system. These compounds are of low abundance, and consistent results were obtained from the skeletal muscle samples.

Instrumentation and analytical conditions
100 metabolites were separated using Waters Acquity ultra performance liquid chromatography, and analyzed using triple quadrupole mass spectrometry as previously described (Roman-Garcia et al., 2014). For folate intermediates analysis, chromatographic separation was done using Atlantis dC18 2.0 X 100mm, 3µ particle analytical column (Waters, Ireland) and the mobile phase was run in gradient mode with flow rate 0.300 mL/min with mobile phase A (formic acid in water 0.1 % v/v) and mobile phase B (acetonitrile). Total analysis time for a single injection was 8.5 min. Column oven temperature and auto sampler temperature was set to 40°C ± 3°C and 5°C ± 3°C, respectively. An injection volume of 5 µL of sample extract was used. The tissue concentrations of folate metabolites were quantified using Xevo® TQ-S tandem triple quadrupole mass spectrometer (Waters, Milford, MA, USA) and electro spray ionization (ESI) was used for positive ion generation $[M+H]^{+}$. Multiple Reaction Monitoring (MRM) acquisition mode was selected for the quantification of metabolites. MassLynx 4.1 software was used for data acquisition, data handling and instrument control. Data processing was done using TargetLynx software.

[U-^{13}C]-glucose flux analysis
For [U-^{13}C]-glucose flux analyses, 20 mg of the labeled glucose (Cambridge Isotope Laboratories Inc, CLM-1396) was administered via tail vein injection into 20-22 months old Deletor mice and age-matched control animals. Tissues were harvested at 5, 10, 15 and 25 minutes; 15 minutes was chosen for further studies based on serine showing linear-phase labeling. Fifteen minutes after injection, animals were euthanized by cervical dislocation; tissues were extracted and snap-frozen in liquid nitrogen. 35 mg of frozen tissue were manually homogenized in 300 µL of 40:40:20 acetonitrile:methanol:water spiked with 1 nM final concentration of D3-^{15}N serine as an internal standard (Cambridge Isotopes Laboratories Inc, DNLM-6863) using a TissueLyser . Homogenate was centrifuged at 15000 rpm for 10 min at +4 °C, and supernatant was separated. Ten microliters of supernatant was used for targeted SRM LC-MS/MS on an Agilent 6460 QQQ fitted with an electrospray source. Metabolites were separated a Luna NH_2 5mm column in normal-phase mode. Mobile phase A was 100 % acetonitrile, mobile phase B was 95:5 water:acetonitrile with either 0.1% formic acid or 0.2% ammonium hydroxide with 50 mM ammonium acetate for positive and negative ionization mode, respectively. Each run started with 100 % A at 0.2 mL/min for 5 minutes, followed by a 15 min gradient from 0% B to 100 % B at 0.7 ml/min and continued with 100 % B for 5 minutes at 0.7 ml/min before equilibrating with 100 % for 5 minutes at 0.7 ml/min. Other settings were: drying gas set to 350°C at 10 L/min, sheath gas set to 400°C at 11 L/min, and the nebulizer was set to 45 psi. Metabolites were analyzed using the MassHunter software package (Agilent Technologies) by quantifying the SRM of the transition from precursor to product ions at associated collision energies.

Supplemental References

Ahola-Erkkila, S., Carroll, C.J., Peltola-Mjosund, K., Tulkki, V., Mattila, I., Seppanen-Laakso, T., Oresic, M., Tyynismaa, H., and Suomalainen, A. (2010). Ketogenic diet slows down mitochondrial myopathy progression in mice. Human molecular genetics *19*, 1974-1984.

Brigelius-Flohe, R., Wingler, K., and Muller, C. (2002). Estimation of individual types of glutathione peroxidases. Methods in enzymology *347*, 101-112.

Gandhi, V.V., and Samuels, D.C. (2011). A review comparing deoxyribonucleoside triphosphate (dNTP) concentrations in the mitochondrial and cytoplasmic compartments of normal and transformed cells. Nucleosides, nucleotides & nucleic acids *30*, 317-339.

Rasanen, I., Viinamaki, J., Vuori, E., and Ojanpera, I. (2010). Headspace in-tube extraction gas chromatography-mass spectrometry for the analysis of hydroxylic methyl-derivatized and volatile organic compounds in blood and urine. Journal of analytical toxicology *34*, 113-121.

Roman-Garcia, P., Quiros-Gonzalez, I., Mottram, L., Lieben, L., Sharan, K., Wangwiwatsin, A., Tubio, J., Lewis, K., Wilkinson, D., Santhanam, B., et al. (2014). Vitamin B(1)(2)-dependent taurine synthesis regulates growth and bone mass. The Journal of clinical investigation *124*, 2988-3002.

Takeuchi, T., Nomura, T., Tsujita, M., Suzuki, M., Fuse, T., Mori, H., and Mishina, M. (2002). Flp recombinase transgenic mice of C57BL/6 strain for conditional gene targeting. Biochemical and biophysical research communications *293*, 953-957.

Traut, T.W. (1994). Physiological concentrations of purines and pyrimidines. Molecular and cellular biochemistry *140*, 1-22.

Xia, J., Mandal, R., Sinelnikov, I.V., Broadhurst, D., and Wishart, D.S. (2012). MetaboAnalyst 2.0--a comprehensive server for metabolomic data analysis. Nucleic acids research *40*, W127-133.

Xia, J., Psychogios, N., Young, N., and Wishart, D.S. (2009). MetaboAnalyst: a web server for metabolomic data analysis and interpretation. Nucleic acids research *37*, W652-660.